

Late Glacial and Holocene Palaeolake History of the Última Esperanza Region of Southern Patagonia

Supplementary Materials and Data

Stephen J. Roberts¹, Robert D. McCulloch², Joseph F. Emmings³, Sarah J. Davies⁴, Wim Van Nieuwenhuyze⁵, Mieke Sterken⁵, Katrien Heirman⁶, Jeroen Van Wichelen^{5,7}, Carolina Diaz⁸, Evelien Van de Vyver^{5,9}, Alex Whittle¹, Wim Vyverman⁵, Dominic A. Hodgson¹, Elie Verleyen⁵

¹British Antarctic Survey, Natural Environment Research Council, Cambridge, United Kingdom;

²Centro de Investigación en Ecosistemas de la Patagonia (CIEP), Coyhaique, Chile; ³British Geological Survey, Nottingham, United Kingdom; ⁴Department of Geography and Earth Sciences, Aberystwyth University, Aberystwyth, United Kingdom; ⁵Protistology and Aquatic Ecology, Ghent University, Gent, Belgium; ⁶TNO—Geological Survey of the Netherlands, Utrecht, Netherlands;

⁷Research Institute for Nature and Forest, Herman Teirlinckgebouw, Brussels, Belgium; ⁸Institute of Ecology and Biodiversity (IEB), Universidad de Chile, Santiago, Chile; ⁹Flanders Environment Agency, Aalst, Belgium.

1. Supplementary Methods

Chronological Methods: Twenty-four samples were taken from the Lago Pato LP08 record and fifteen samples from the LP16 record for Accelerator Mass Spectrometry (AMS) radiocarbon dating. For the LP08 record, these included five highly organic macrophyte-dominated lake-mud samples, which were wet-sieved (250 µm) to remove fine mineralogenic sand, silt, and clay particles; six organic-rich bulk lake-mud samples; three hand-picked plant macrofossils; seven fine glaciogenic bulk sediment samples. The LP16 samples consisted of four hand-picked plant macrofossils, five organic peat/lake mud bulk samples and five glaciogenic bulk sediment samples (Table 3).

Radiocarbon dating samples analysed by SUERC were ‘acid-washed’: digested in 2 M HCl (80°C for 8 hours), washed free from mineral acid with distilled water until all traces of acid and carbonate had been removed, and dried in a vacuum oven. The total carbon in a known weight of all pre-treated samples was recovered as CO₂ by heating with CuO in a sealed quartz tube. The CO₂ was converted to graphite by Fe/Zn reduction. Samples dated by Beta Analytic were ‘acid-washed’: leached with a 0.5M to 1.0M HCl bath to remove carbonates, heated to 70°C for 4 hours. Leaching was repeated until no carbonate remained, followed by rinsing to neutral 20 times with deionised water. Plant material samples were ‘acid/alkali/acid’ pretreated using the above procedure then placed in 0.5% to 2% solution of NaOH for 4 hrs at 70°C and rinsed to neutral 20 times with deionised water. The process was repeated until no additional reaction (typically indicated by a colour change in the NaOH liquid) was observed. Samples were then leached again in a 0.5M to 1.0M HCl bath to remove any CO₂ absorbed from the atmosphere by the NaOH soakings and to ensure initial carbonate removal was complete. All samples were dried at 70°C in a gravity oven for 8-12 hours.

Calibration of measured radiocarbon ages was undertaken in OXCAL v.4.2 (Ramsey, 2009) using the SHCal20.14C Southern Hemisphere atmosphere dataset (Hogg et al., 2020). Post-bomb samples were calibrated using the SHCal13 SH Zone 1-2 Bomb curve in CALIBomb (Hua et al., 2013). Radiocarbon age data are reported as conventional radiocarbon years BP (¹⁴C yr. BP) $\pm 1\sigma$ and as 2 σ (95.4%) calibrated age ranges, median and mean cal yr BP (relative to 1950 CE) (Table 3), rounded to the nearest ten years as measured age errors are less than ± 50 ¹⁴C years. Age-depth models were generated using Bayesian age-depth modelling software BACON v.2.5 (Blaauw and Christen, 2011)

using R v. 3.5. Weighted mean interpolated ages, derived from the ‘best-fit’ age depth model, and 95% confidence interval calibrated age ranges were rounded to the nearest 100 years in the text to reflect dating errors and modelling uncertainties. Holocene sediment accumulation rates in LP08 were relatively uniform apart from a notable decrease in the less-compacted uppermost 40 cm. The minimum-maximum range and mean $\pm 2\sigma$ sedimentation rate from 470 cm upwards is 0.011–0.085 cm yr⁻¹ and 0.055 ± 0.04 cm yr⁻¹ meaning that a 1 cm sampling interval represents, on average, 18 years and a 2 mm interval represents 4 years. Accumulation rates are highest during the mid-late Holocene (0.05–0.08 cm yr⁻¹ and lowest during the early Holocene (340–470 cm; 10,000–6,100 cal a BP: 0.025–0.05 cm yr⁻¹) and during the last c. 1,500 years (upper 40 cm: 0.025–0.03 cm yr⁻¹).

Core Scanning Methods: Cores were split and analysed using a GEOTEK multi-sensor core logger following standard procedures to obtain gamma-ray density, resistivity and magnetic susceptibility (MS) data (Gunn and Best, 1998) (Bartington Instruments; LP08: MS2C loop sensor, 2 mm intervals, 10 seconds; LP16: MS2E point sensor, 0.5 mm intervals; 10 seconds). XRF core scanning (XRF-CS) analysis was undertaken to characterise bulk wet geochemical variations. Digital X-radiographs were obtained from split cores using a rotating anode mobile digital Celtic SMR CR computerised X radiography unit, based at Cambridge University Vet School (48kV; 4 mAs; no grid; exposure per plate digitally processed and converted to JPEG files) and, prior to XRF-CS analysis, from an ITRAX™ digital X-radiograph (45 kV, 50 mA.ms, 200 ms, 60 μ m interval) at the University Aberystwyth. Contiguous downcore wet-sediment Energy Dispersive Spectrometry (EDS) XRF-CS geochemistry was obtained using an ITRAX™ XRF scanner fitted with a Molybdenum (Mo) anode X-ray tube (settings: 30 kV, 50 mA, count time 10 seconds, at 2 mm (Unit 6 LP08), 200 μ m (Unit 1 LP08) 100 μ m intervals (basal Unit 1; core LP08-1I), and LP16 (0.5 mm (Units 2-6) and 200 μ m Unit 1) intervals). A synthetic glass standard and XRF fused glass discs from Antarctic lake sediment core subsamples were used to ensure the XRF-CS scanner was functioning correctly.

XRF-CS spectra were analysed using Q-spec v8.6.0, to generate count per second ED (Energy Dispersive) datasets with MSE values minimised to optimise measured-modelled spectra fit and generate robust counts-per-second (cps) data. To account for downcore variations in water content and density, and to examine covariance, closed-sum effects, and non-stationarity of some geochemical responses through time, data were normalised by total scatter cps (incoherent (Compton) scatter + coherent (Rayleigh) scatter). Results are expressed as log₁₀ and/or natural log element/total scatter ratios, and as a percentage of the total scatter normalised ratio (\sum TSN; see below) (Kylander et al., 2011; Davies et al., 2015; Roberts et al., 2017; Saunders et al., 2018). As Al counts were too low (Löwemark et al., 2011) and Rb counts in organic-rich deposits were often zero (Wilhelms-Dick et al., 2012), Ti-normalised (natural) log-ratios were used to estimate of the background bedrock composition. Constrained CONISS clustering of XRF-CS geochemical data was used to delineate lithofacies zones. Principal Components Analysis (PCA) was used to establish correlation relationships between different elements and determine which element ratios could be used to constrain lake orogeny, sediment provenance, and bottom water redox conditions. Data from finely laminated glaciolacustrine sediments in Units 1 and 2 were smoothed to 200 μ m and equal spaced time-intervals (10-years and 100-years) used for time series analysis were centered, standardised (Z-scores) and detrended (polynomial linear best fit) and interpolated using a 10-year Piecewise Cubic Hermite Interpolating Polynomial (PCHIP) interpolation applied to avoid spline artefacts and preserve the shape of the original XRF-CS data series. Second order polynomial Locally Weighted Scatterplot Smoothing (LOESS) 100-year smoothing (0.1 sampling interval with outliers removed) was also used to compare datasets to published data.

Detection limits are <c. 1% for all elements described. For direct comparison with 1 cm interval subsample data, five-point and 50-point cps data sum and ratio/percentage running means were used to convert 2 mm and 200 μ m as-measured interval datasets to 1 cm in intervals. The 1 cm dataset is equivalent to 50 and 500 second scans per cm, respectively, and allowed the more reliable acquisition of useful light elements with low count rates, e.g., Si, P and S. Improved counting statistics for these lighter elements can also be obtained using Cr-tube analysis (Saunders et al., 2018) (not undertaken

on the Lago Pato cores). Elemental and scatter counts were calculated from measurable element peak area count per second data (cps). After filtering out low-count areas and spurious data due to uneven sediment surface or gaps in the core with lower-than-average count statistics (<2-sigma standard deviation kcps), CONISS (constrained) cluster analysis was applied to 1 cm mean datasets to identify geochemically distinct zones.

XRF-CS Total Scatter Normalisation: XRF core scanning has many advantages, but it is an Energy Dispersive Spectrometry (ED) method and, therefore, produces semi-quantitative, non-concentration data. Without normalisation, trends in wet sediment XRF-CS scan data can be different to those obtained by standard (whole-rock composition) XRF analysis in which water and carbon are removed beforehand. Potential differences between Wavelength Dispersive Spectrometry (WD)-XRF and EDS XRF-CS techniques can be undertaken by examining data from representative lithologies using WD-XRF and ICP-MS subsample analysis methods. Several examples good coherence between ED XRF-XRF and WD-XRF methods can be found in (Rothwell and Croudace, 2015). Since we are primarily interested in the downcore trends in wet sediment and the differences between organic-rich and minerogenic sediments, scan data have not been calibrated using subsample data in this study (Davies et al. 2015). XRF-CS data were compared with downcore patterns of standard palaeolimnological parameters (e.g., LOI, TOC, MS). Further comparison of the patterns obtained from ED and WD techniques is outside the scope of the present study and was largely ineffectual in highly organic Holocene-age deposits in the LP08 and LP16 records.

Without normalisation, spurious elemental patterns and matrix effects can occur in wet sediment scanning, especially when dealing with a high and/or highly variable highly organic sediment content (Croudace et al., 2006; Wilhelms-Dick et al., 2012; Davies et al., 2015). To account for these effects, closed-sum effects and downcore variations in organic and water content, and to allow comparisons between cores run at different times and different tube life, cps data were normalised by total scatter counts (incoherent+coherent) (Kylander et al., 2011; Löwemark et al., 2011; Davies et al., 2015) and element/Ti log ratios to account for closed-sum effects associated with compositional data.

To determine the relative proportions of individual elements and scatter parameters measured and examine covariance patterns, we examined scatter ratios (element/in.) and expressed element/inc.+coh. values (following Kylander et al., (2011)) as a percentage of the total scatter normalised element and scatter cps ratio sum ($\sum\text{TSN}$). Total scatter ($\sigma_{\text{inc}+\text{coh}}$) (cps) is defined as Compton+Rayleigh scattering and referred to as incoherent (σ_{inc}) (Compton or inelastic) +coherent (σ_{coh}) (Rayleigh or elastic) scattering. In effect, this method accounts for the influence of scatter, by converting it to a constant equal to one.

Elemental and scatter data in this study are presented as percentages of the Total Scatter Normalised ratio sum (% $\sum\text{TSN}$ or, simply, %TSN), which produces the same percentage values for elements and scatter expressed as a percentage of the cps sum (%cps). Scatter normalisation %TSN and %cps methods provide a simple and effective way to account for the influence of variable scatter from wet (and organic-rich) sediment and can produce different downcore profiles to cps plots and. These percentages are tube-specific and represent the proportion of elements measured by ITRAX™ ED XRF-CS analysis and are not equivalent to whole rock compositions obtained by traditional XRF analytical techniques.

Correlations between key elements and parameters of interest were determined using Pearson Correlation Coefficients (PCC) (Table S1) and by Principal Components Analysis (PCA). Covariant element and scatter parameters are colour-coded in Figures S2 and S3 according to their PCA axis 1 derived relationship to minerogenic (blue) or organic-driven (green) trends. Covariance and PCC statistics were used to determine which of the recognised ‘stable’ elements can be considered resilient to weathering processes (e.g., Al, Ti, Rb; Davies et al. (2015)) had sufficient counts for normalization. Al and Rb cps were considered too low for reliable normalization, particularly in organic-rich sections of the record.

In calibration tests, trends in reliably measurable downcore elements (e.g., Ti) have been well correlated to traditional XRF subsampling methods (e.g., Roberts et al., 2017). We also compared %TSN element and scatter with those obtained using the Boyle et al. (2015) dry mass ‘concentration’ normalization method where elemental and scatter cps data are normalized by the $\sigma_{coh}/\sigma_{inc}$ ratio to produce dry mass equivalent datasets. These important initial data processing steps were particularly important for elements such as Mn, Fe, Ca in this study that have multiple possible sources (Kylander et al., 2011; Melles et al., 2012).

Cryptotephra analysis: Glass shard geochemistry was analysed using the Cameca SX-100 electron probe microanalyser (EPMA) at the Tephra Analytical Unit, University of Edinburgh by Chris Hayward with a beam diameter of 8 μ m following procedures in Hayward (2012) and run conditions: 15 keV/2 nA (Al, Ka, Si Ka, K Ka, Ca Ka, Na Ka, Mg Ka, K Ka, Ca Ka, Fe Ka); 15 keV/80 nA (P Ka, Ti Ka, Mn Ka, P Ka, Ti Ka). Andradite standards were run at the start and end of each session. Analytical conditions and results for shards with >95% totals are shown in Table S2. New shard geochemical data was compared to a database of distal tephra major element glass shard analyses from Southern South America n = 1,031 (McCulloch and Davies, 2001; McCulloch et al., 2005; Sagredo et al., 2011; Stern et al., 2015; Mansilla et al., 2016; McCulloch et al., 2017; Mansilla et al., 2018; McCulloch et al., 2019; Smith et al., 2019; Blaikie, 2020; McCulloch et al., 2020; McCulloch et al., 2021) using Principal Components Analysis (PCA) and k-means hierarchical cluster analysis (Wards method, Euclidean distance between samples).

Diatom analysis: Several different sources were used for diatom taxonomy (Rumrich et al., 2000; Guerrero and Echenique, 2002). For some diatom identifications, scanning-electron microscopy was used in addition to light microscopy. Some species were grouped or could only be identified to genus level because of difficulties in distinguishing morphotypes/species under light microscopy, for example *Fragilariod* species.

Statistical analysis: Hierarchical cluster analysis (k-means; Ward’s) and data plotting was undertaken in RStudio v. 0.98.939 using R v. 3.5 and packages Vegan v. 2.3-0 (Oksanen, 2014) and Rioja v. 0.8-5 (Juggins, 2012), XLStat v. 2010.3.09, C2 v. 1.7.6 (Juggins, 2007), C2 v. 1.7.7, and SigmaPlot v.14. Principal Components Analysis (PCA) was undertaken in C2 and R using packages ggplot2, factoextra, dendextend, cowplot, Ggally and ITRAX.r (Bishop, 2021)) with standardised (mean- 1σ) and centered natural log-transformed percentage diatom, pollen and %TSN XRF-CS data. CONISS stratigraphically constrained cluster analysis with Hellinger’s distances was undertaken in R packages Rioja and Tilia (Grimm, 1987) on standardised (mean- 1σ) percentage data with broken stick analysis to determine the stratigraphic position of significant geochemical, diatom and pollen units/zones. Time series (interpolation, standardization (Z-scores), detrending, autocorrelation, peak identification, changepoint and wavelet analysis) were all undertaken in MATLAB using standard Signal Processing Tools and modules.

All data has been deposited in the NERC EDS UK Polar Data Centre (PDC) as follows:

Roberts, S., Sterken, M., Heirman, K., Van Wichelen, J., Diaz, C., Vyverman, W., & Verleyen, E. (2022). Bathymetric and lake chemistry data for Lago Pato, Torres del Paine National Park, Chile (Version 1.0) [Data set]. NERC EDS UK Polar Data Centre. <https://doi.org/10.5285/D55D7619-3E07-41B0-929E-C9DA0A4B61AF> Short DOI: <https://doi.org/hjnx>

Roberts, S., McCulloch, R., Davies, S., Emmings, J., Sterken, M., Van de Vyver, E., Van Nieuwenhuyze, W., Heirman, K., Van Wichelen, J., & Diaz, C. (2022). Biological, chronological, geochemical, and physical sedimentological data for the LP08 lake sediment record extracted from Lago Pato, Torres del Paine, Chile in 2007-2008 (Version 1.0) [Data set]. NERC EDS UK Polar Data Centre. <https://doi.org/10.5285/C75EA98B-080E-455E-A54F-A9E8CF07AA73> Short DOI: <https://doi.org/hjnz>

Roberts, S., McCulloch, R., Emmings, J., Davies, S., Vyverman, W., Verleyen, E., & Hayward, C. (2022). Biological, chronological, geochemical, and physical sedimentological data for the LP16 lake sediment record extracted from Lago Pato, Torres del Paine, Southern Chile in 2015 (Version 1.0) [Data set]. NERC EDS UK Polar Data Centre. <https://doi.org/10.5285/F85EE4EB-8918-4AA4-8E51-6C46F4C812CB> Short DOI: <https://doi.org/hjn2>

Roberts, S., McCulloch, R., Emmings, J., & Davies, S. (2022). Geochemical X ray fluorescence log ratio time series data for two sediment cores, LP08 and LP16, extracted from Lago Pato, Torres del Paine, Southern Chile (Version 1.0) [Data set]. NERC EDS UK Polar Data Centre. <https://doi.org/10.5285/6BD95602-F2E3-4968-8622-C4AEB71C214C> Short DOI: <https://doi.org/hjn3>

Code and data can be found at: https://github.com/stever60/Lago_Pato.

2. Supplementary Results

Chronological Results: Four radiocarbon ages from organic deposits in LP08 and LP16 were outliers due to the emplaced during coring and excluded prior to age-depth modelling (Table 3). In LP08, flocculent organic deposits recovered from >600 cm depth with radiocarbon ages of <9,000 cal yr BP were emplaced by upwards suction on extraction of the core from Unit 1 deposits and not considered part of the sequence stratigraphy. Translocated root material in Unit 2 of LP16 with a significant age reversal was rejected as an outlier and excluded from the LP16 age-depth model.

As-measured results from both records imply that a deep palaeolake existed at Lago Pato between the gLGM and local glacier maximum extent, and that sediments between c. 21,000–10,000 cal a BP are missing from the LP08 record. In contrast, no obvious evidence of a hiatus due erosion by glacier overriding or rapid lake emptying exists between Units 1 and 2 in the LP16 stratigraphic record.

For Units 1 and 2 in LP16 to be continuous, bulk radiocarbon ages would require a lake reservoir correction of c. $6,600 \pm 500$ ^{14}C years. Problems with ‘old’ carbon glacially derived sediments in the TdP region are well-documented (McCulloch and Davies, 2001; Solari et al., 2012; Davies et al., 2020) and bulk dates are widely considered to represent maximum, rather than depositional ages of palaeolake formation (Grimm et al., 2009; García et al., 2014). Several processes are known to create offsets of as much as 10,000 years in glaciolacustrine sediments: 1) carbonate or ‘hard water effect’; ‘old’ carbon by glacial erosion; radiocarbon-depleted glacial meltwater; 2) reduced gaseous exchange at the sediment water interface in deep and poorly ventilated lakes; 3) perennial ice cover; disturbance of the sediments by ice or ice-rafting (Hodgson et al., 2009).

A large reservoir-correction for Unit 1 sediments is supported by an offset of c. 3,640 years between two closely spaced bulk sediment samples at 554–555 cm and 556–557 cm in LP08 (Calibrated ages of $22,740 \pm 120$ cal yr BP and $26,380 \pm 190$ cal yr BP; Table 3). Conversely, mean %TSN values for Ca in LP08 and LP16 Unit 1 deposits are <2% and maximum values in Unit 6A are significantly lower (Ca<15%TSN) than marl deposits in other lake records from Patagonia (Ca>70%TSN; McCulloch, unpublished data), suggesting ‘hard water’ corrections for bulk radiocarbon ages may not be necessary. All other carbonate proxies (LOI_{950} , resistivity, Ca/Ti, Sr/Ti) remained low in Unit 1 in LP08 and LP16 and in Unit 2 in LP16 compared to Units 3–6A/B in both records. Carbon isotope data of Unit 1 sediments from both records were only marginally enriched (mean $\pm 1\sigma$: n = 16, % C_{org} = 0.69 ± 0.54 , C/N = 8.00 ± 1.10 , $\delta^{13}\text{C} = -26.28 \pm 1.56 \text{ ‰}$ and $\delta^{13}\text{C}$ dated: n = 11; $-25.2 \pm 0.3 \text{ ‰}$) compared to the glacial sediments of Unit 2 ($\delta^{13}\text{C}$ from radiocarbon dated samples n = 2; $-29.3 \pm 3.0 \text{ ‰}$) and Holocene-age organic deposits and macrofossils (mean $\pm 1\sigma$: n = 101, % C_{org} = 21.66 ± 8.60 , C/N = 11.34 ± 0.90 , $\delta^{13}\text{C} = -30.15 \pm 1.13 \text{ ‰}$ and $\delta^{13}\text{C}$ dated: n = 19; $-28.9 \pm 1.3 \text{ ‰}$). N/C ratios corrections are not generally applicable to ‘carbonate-rich’ lakes in Chilean Patagonia environments

influenced by hard water effects (Bertrand et al., 2012) yet Holocene-age offsets during exceptionally arid phases between 10–7.5 ka are minimal, with a mean N/C-based age correction for Unit 6 deposits of 25 ± 2.5 years.

Cryptotephra analysis: The LP16 record contains two visible Holocene tephra deposits, between ~35–32 cm ($5,720 \pm 130$ – $3,970 \pm 230$ cal yr BP), and between 13–12 cm (540 ± 220 – 420 ± 300 cal yr BP). The age of the LP16: 35–32 cm tephra is consistent with a prominent cryptotephra peaks at ~252 cm (4740 ± 130 cal yr BP) in the LP08 record (Figure 5, S2). A further cryptotephra deposit, also characterized by MS, Ti, Sr, Si peaks within the organic matrix layer, occurs at ~29–25 cm (3020 ± 180 cal yr BP). EPMA data produced thus far from glass shards at 12.5, 32 and 57 cm depth in the LP16 record produced mixed results with no clear match to known eruptions (Figure S9, S10). In common with some other records from the Torres del Paine and peat records from further south in Patagonia, EPMA analysis of cryptotephra undertaken thus far shows a large geochemical spread, broadly affiliated to the Austral Volcanic Zone (rhyolitic), but with no individual deposit correlating convincingly with any of the major Holocene eruptions of Reclus, Aguilera, Burney, or Hudson in the Southern Volcanic Zone (Andesitic). No Holocene-age ash layers were visible in the LP08 record and, thus far, we have found no (crypto)tephra of a similar age to the Hudson H1 tephra at c. 8,700 cal yr BP (Smith et al., 2019). Cryptotephra in the LP08 record between 338–334 cm ($6,140 \pm 540$ – 5980 ± 480 cal yr BP) is characterized by peaks in MS, Ti, Sr, Si within the organic matrix (Figure 5A, S2). This could possibly relate to the ChaA1 eruption of the Chaitén volcano (>6000, but <7450 cal yr BP) (Fontijn et al., 2014), which deposited ash southwards across Patagonia but this requires further investigation.

Core Scanning Results: For Mo-tube 2 mm datasets with 10 second count time, Al and Rb cps were considered too low for reliable normalization, particularly in organic-rich sections of the record; hence, we present data as total scatter-normalised and element/Titanium (Ti) normalized percentage ratios and \log_{10} or natural log-ratios (Figure 5, 6, 8, 10, S2, S3). The LP08 2 mm dataset (mastercore, filtered data) has a mean $\pm 1\sigma$ kcps = $18,776 \pm 3218$ and mean MSE = 1.33 ± 0.12 ($n = 2885$), the LP08 200 μm -2 mm dataset has a mean $\pm 1\sigma$ kcps = $16,187 \pm 2606$ and mean MSE = 1.28 ± 0.10 ($n = 9059$); the LP16 2 mm dataset has a mean $\pm 1\sigma$ kcps = $21,080 \pm 2441$ and mean MSE = 1.47 ± 0.11 ($n = 1444$) and the LP16 200 μm -2 mm dataset has a mean $\pm 1\sigma$ kcps = $20,778 \pm 2187$ and mean MSE = 1.50 ± 0.13 ($n = 10,712$). The TSN ratio sum for LP08 is correlated with coh./inc. and both relate to changes in dry mass (Boyle et al., 2015) (r values >0.80; $p < 0.0001$) (Figure S4; Table S1). Other correlations between key variables from subsample and XRF-CS data are summarised in Table S1. Downcore PC axes 1 and 2 explain 67.5% and 11.7% of the variance in the LP08 2 mm dataset and 67.8% and 12.5% of the variance in the LP16 200 μm -2 mm dataset (Figure S2, S3).

The LP08 and LP16 records were divided into six lithofacies units shown in Figure 5, Table 2 and summarised as follows:

Unit 1: Unit 1 is characterised by high to moderate MS, high Ti, Rb, with high and stable Fe/Mn and Sr/Ca associated with glaciogenic physical weathering products and allochthonous catchment erosion (Figure 5). Low organic matter (including Br) content, together with a lack of authigenic enrichment of redox-sensitive trace elements (e.g., V/Ti), suggests deposition under low productivity and generally well-ventilated bottom water conditions. Unit 1 represents the ‘background’ glaciogenic detrital composition, with well-developed fine scale internal structure, most notably within Unit 1A (Figure 6B–F). Fe/Mn and Mn/Ti ratios are inversely related in LP08 in general ($r = -0.65$; $p = 0.0047$) and within Unit 1, with well-developed decadal to centennial scale variability present between the Ti- and Ca-rich orange-grey and light grey laminations (Figure 6B–F).

Units 2–4: The detrital component of Unit 2 is composed of light grey (glaciogenic) silty clay, similarly enriched in Ti, K, Fe and Mn to Unit 1, but massive and embedded with subaqueous *Myriophyllum* sp. fragments. Unit 3 is composed entirely of shallow water sub-aquatic *Myriophyllum* sp., an early colonizer (Figure 5B). The moderate to low MS and Ti and elevated Br content of Unit

3 implies declining input of glaciogenic physical weathering products and increase in the organic matter content, biogenic activity, and productivity in the lake. Unit 4 is similar to Unit 2 but distinguished by substantial enrichment in Ca and Sr (but not S) and a lower density of *Myriophyllum* sp. fragments (Figure 5B).

Units 5–6: Unit 5 is structureless organic lake mud characterized by very low MS, low Ti content, high Br (and other organic proxies) and higher (more terrestrial) C/N values than Unit 1, which reflect increased productivity in a shallower basin. Unit 5A in LP16 has extremely high Fe/Mn ratios which reflect an ‘Anoxic Crisis’ during a period of lower water levels (and possibly peat formation), as conditions became and calmer and more stable at the LP16 site. Units 5B–C between c. 10–5.6 cal ka BP are characterised by increased erosional inputs (shown by elevated MS and Mn/Ti), with Fe/Mn remaining low and occasional exceptionally elevated Ca and S in LP08 (Figure 5A), whereas, in LP16, MS remained low, with significantly increased Mn/Ti and Fe/Mn (Figure 5B). Unit 6 is a highly organic, structureless and increasingly fibrous macrophytic lake mud depleted in low detrital elements, with low Mn/Ti and increasing Fe/Mn ratios (more anoxic/stable) in LP08 and decreasing Fe/Mn ratios in LP16 (more oxic/less stable).

We classified element and element/total scatter ratios into five groups:

- 1) *Catchment erosion proxies:* Here, we used: >Ti/inc.+coh. >coh./inc. ratio and >MS as proxies for increasing detrital clastic (minerogenic) input; >(Fe+Ti)/K or Ti/K as a grain size indicator, compared to the clay fraction with >Rb/Ti reflecting increased clay input (Davies et al., 2015); >Sr/Ti for increased detrital input during the glaciogenic sediments and soil erosion in the non-glacial deposits, coupled >Si/Ti, >K, >Ti, >MS to identify tephra deposits; concomitant >Sr/Ti + >Si/Ti to identify outwash sands; coupled >Mn/inc.+coh., >Fe/Ti, >Mn/Ti, >MS in glaciolacustrine deposits to identify magnetite-rich sediments and erosional layers and >Mn/Ca and >MS to locate cryptotephra deposits.
- 2) *Redox proxies:* Elevated Fe/Mn and Mn/Ti ratios have been interpreted as representing increased stability and anoxia, which, combined with <Ca/Ti and <Sr/Ti, reflect increased water depth in Lago Pato. This is because Mn²⁺ is more stable in pore water and precipitates later than Fe²⁺, while Mn is more soluble than Fe in anoxic conditions, leading to lower Fe/Mn ratios in sediment profiles during periods of lake anoxia (Wennrich et al., 2014; Davies et al., 2015). Although Fe has many potential sources, including detrital inputs, elevated Fe counts often reflect increased water column stratification and anoxia in very deep and otherwise unproductive proglacial lakes, and a lack of mixing in more productive and shallower lakes (Kylander et al., 2011). Hence, higher Fe/Mn ratios reflect greater stability and stratification. High Mn and magnetite solubility also occur in more anoxic conditions, particularly at depth and with perennial lake ice-cover, associated with colder glacial conditions (Melles et al., 2012; Olsen et al., 2013; Wennrich et al., 2014; Davies et al., 2015). Conversely, higher Mn/Ti and <Fe/Mn ratios have been widely used as indicators of increased oxidation, particularly where wind-driven mixing of the lake water column in deep water and glaciolacustrine environments or in shallow-dry lakes overturns stratification and reduces Mn solubility causing manganese oxides and hydroxides to co-precipitate with iron oxy-hydroxides (Wennrich et al., 2014; Davies et al., 2015). Elevated S/Ti in Units 6C and D has a strong association with elevated Br/Ti ($r^2 = 0.91$; Figure S4F). In most non-marine environments, and in Lago Pato, Br has a particularly strong association with organic material and lower Fe/Mn ratios (Davies et al., 2015). An exception occurs in shallow-littoral organic (possibly terrestrial deposits) (e.g., LP16 Units 4–5) where exceptionally elevated Fe/Mn ratios, reflecting a very anoxic environment (‘Anoxic crisis’ in Figure 5, 8, 10), are covariant with elevated inc./coh., Br and S ratios (Figure 5, 6A). The shallow water organic-rich environments of Units 5A and B have higher S/inc.+coh. and S/Ti ratios than Units 1 and 2 (Figure S4), reflecting increased eutrophication-driven anoxia, limited ventilation, and greater stability.

- 3) *Carbonate deposition proxies*: We identified the following modes of Ca- and carbonate-deposition:
- i. *Minerogenic, catchment-derived Ca*: In this mode, Ca is principally covariant with erosional elements. Relatively low Ca content throughout Unit 1 is associated with the low-Ca and high-Rb content of fine clays eroded from an enlarged catchment.
 - ii. *Minerogenic Sr- and Ca-rich*: Elevated Ca and Sr between, for example, ~42-43 cm in LP08 are caused by the inwash of fine sandy-silt minerogenic Sr-rich deposit (labelled S, in Figure 5A). All major measurable minerogenic elements (K, Ti, Fe, Rb, Sr, Ca) are significantly elevated above background organic values, distinguishing Sr and Ca peaks from those formed by cryptotephra. The similarity between paired ages from bulk organic mud and plant remains between 41–40 cm indicates minimal carbonate impact on radiocarbon ages.
 - iii. *Authigenic carbonate (evaporation and precipitation related)*. In this mode, elevated Ca is associated with Sr and S. Precipitation of calcite, carbonates and, eventually, evaporites progresses rapidly in some closed, cold-water, high latitude and/or density-stratified (heliothermal-hypersaline) lacustrine environments (Lauterbach et al., 2011; Jouve et al., 2013; Olsen et al., 2013). Elevated Ca and S in combination have been associated with formation of CaSO_4 (gypsum) (Brown, 2011; Hodell et al., 2012; Mueller et al., 2017), common in semi-arid environments of the northern high Andes with a dry steppe climate (Farias et al., 2014). Carbonate-rich evaporation rinds exist around ion-concentrated, closed-shallow brackish lakes in Southern Chile (Campos et al., 1995).
 - iv. *Anoxia*: This mode occurs where elevated S conditions become decoupled from Ca during stratification, suggesting anoxic (and poorly ventilated) conditions developed as in-lake productivity rose (Kylander et al., 2011)
- 4) *Organic proxies*: Incoherent/coherent (inc./coh._{Mo}) ratios obtained from Mo-tube analysis reflect changes in water content and sediment density in the LP08 and LP16 records, and have been used as proxies for organic content (%TOC and/or Loss-on-ignition) (Jouve et al., 2013; Davies et al., 2015; Roberts et al., 2017). Organic material is less dense, and more water saturated, and higher inc./coh._{Mo} ratios show a strong and significant correlation with >TOC and >Br (inc/coh – TOC: $r^2 = 0.94$, Br-TOC: $r^2 = 0.84$; $p < 0.0001$ for both; Figure 5A; Figure S4).
- 5) *Matrix effects*: These occur when scanning wet, organic-rich deposits (Kylander et al., 2011; Davies et al., 2015). Elevated levels of Zr are commonly found in sand-size grains and variations in Zr have been used as a proxy for changes in grain-size elsewhere. While stable values in Unit 1 in both records reflect the consistently fine-grained minerogenic nature of (glaciolacustrine) sediments deposited, elevated Zr values in the more organic-rich units 5 and 6 most likely represent a matrix effect caused by Zr being adjacent to the Mo-incoherence peak in the energy spectra (Figure S5).

Diatom analysis: Where possible, a distinction was made between different morphotypes in the groups of the small benthic *Fragilariod* species (e.g., *Staurosirella* aff. *pinnata*; *Staurosira* aff. *venter*) (Figure S7). These groups may be the same species but still exhibit different ecological responses. Further studies are needed to understand these distinct ecological shifts within the *Fragilaria* species in general, and, more specifically, in the LP08 and LP16 records (Figure S7) (Einarsson et al., 2004; Finkelstein and Gajewski, 2008; Bennion et al., 2010) since the full significance of these shifts is not currently understood (Westover et al., 2006; Bennion et al., 2010). Nevertheless, the size and shape of valves within one diatom species can reflect different environmental conditions (Stevenson et al., 1999; Stevenson et al., 2010).

3. Supplementary Figures

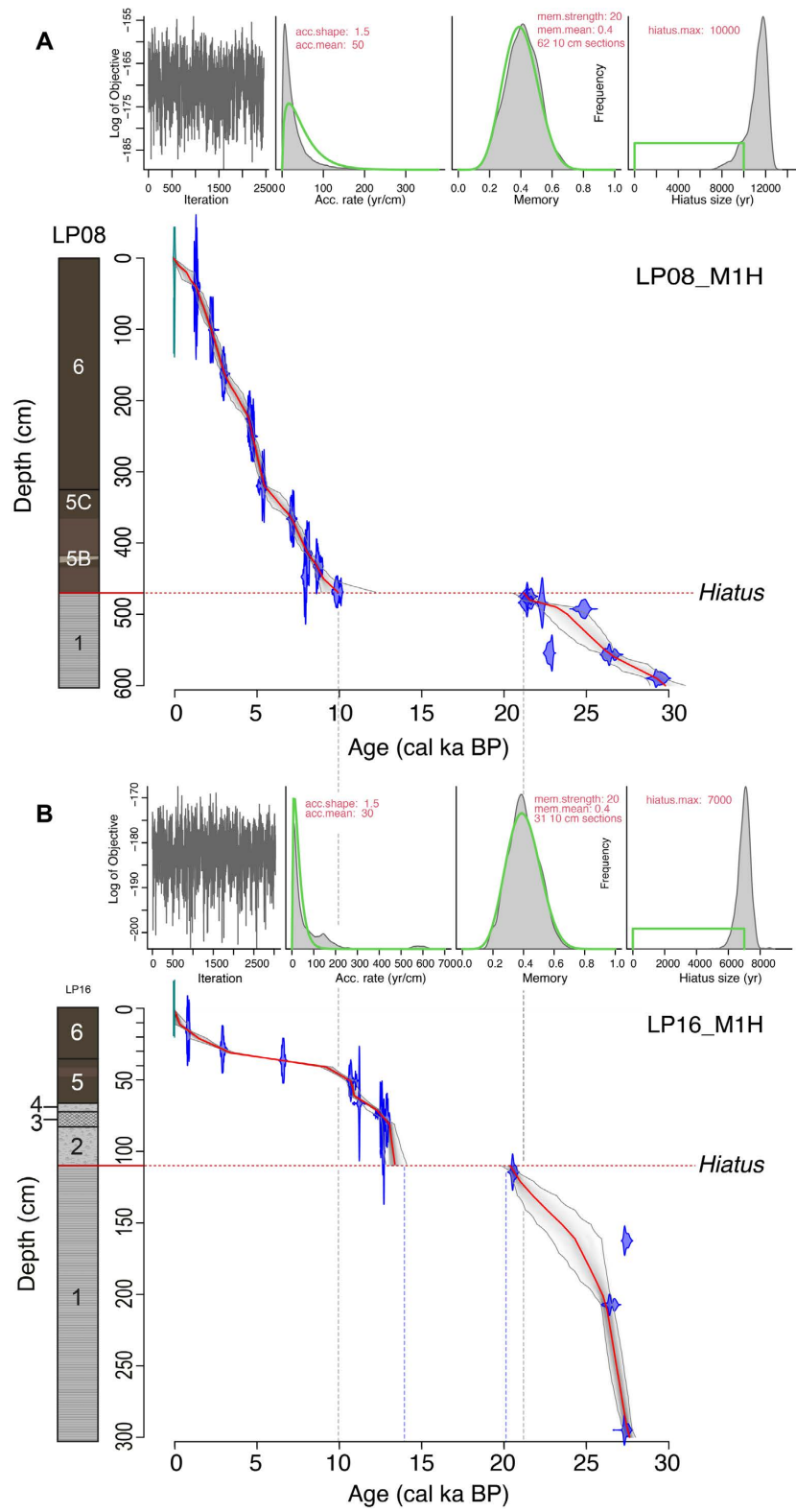


Figure S1. Summary of age depth models for Lago Pato sediment records **(A)** LP08 and **(B)** LP16 constructed using BACON v.2.4 (Bayesian) age-depth modelling software in R v3.1 using the SHCal120.14C Southern Hemisphere atmosphere dataset (Hogg et al., 2020). Prior settings are shown in the inset boxes. Data and code can be found at: https://github.com/stever60/Lago_Pato.

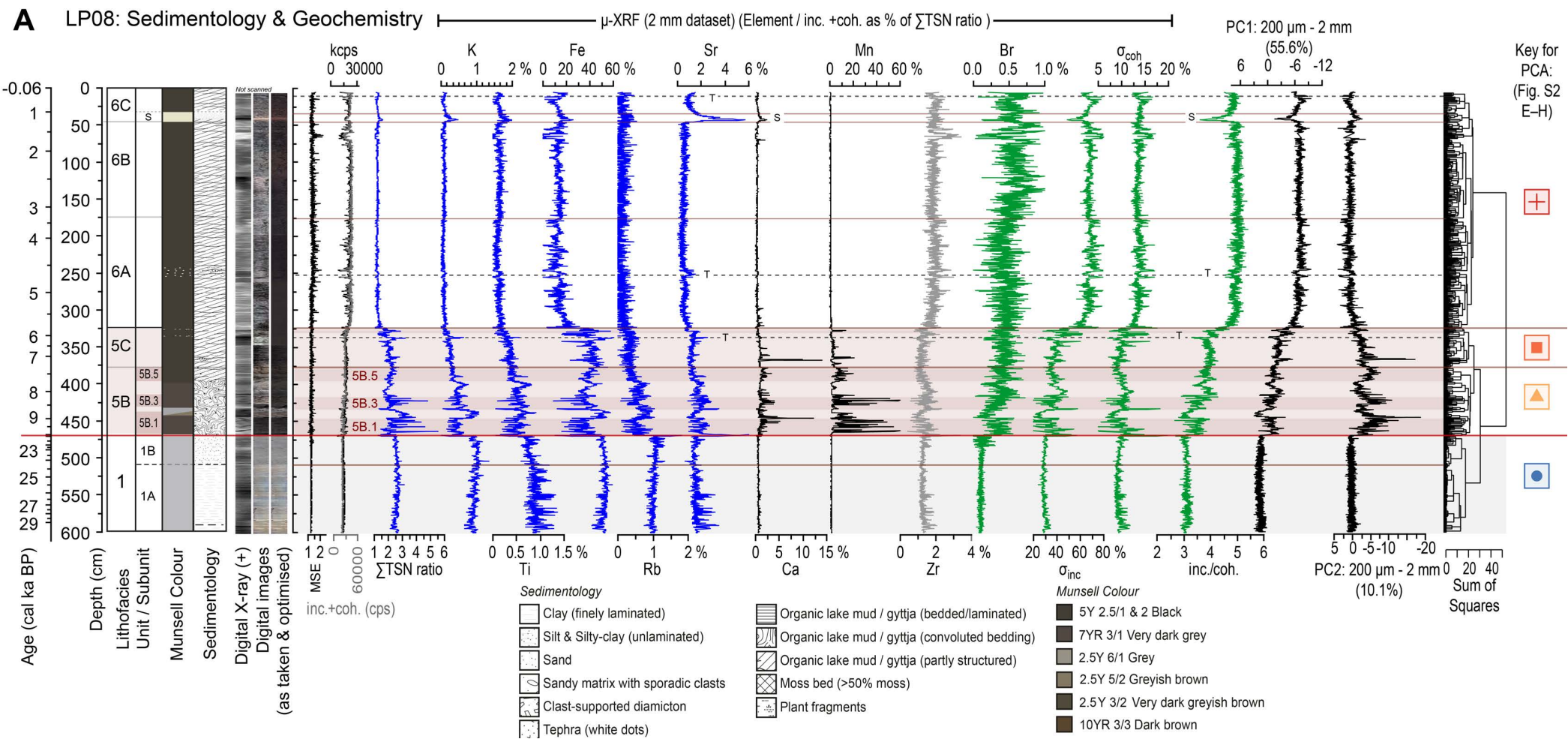
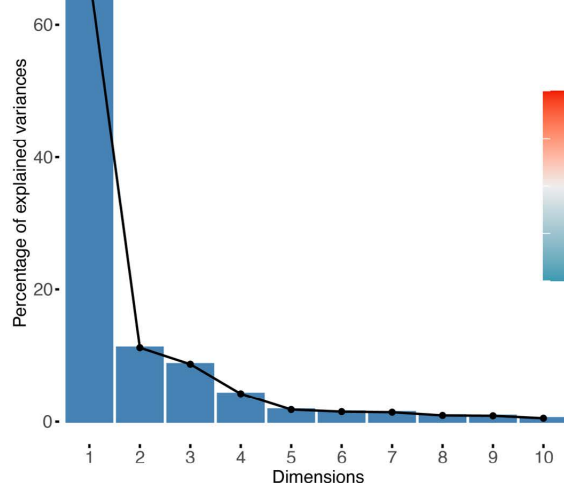


Figure S2. (A) Summary sedimentological logs and downcore XRF-CS composite 2 mm dataset for the Lago Pato sediment record. Plot colours for elements and scattering parameters reflect minerogenic versus organic affinities. Blue plots have a significant and strongly positive relationship to TSN ratios (Pearson correlation coefficient (PCC) $r>0.5$; $p<0.0001$; $R^2>0.5$) and a significant negative relationship with inc./coh. ratios (PCC <-0.5 ; $p<0.0001$; $R^2>0.5$). Green plots are positively correlated with inc./coh. ratios., while black plots show no strong relationship to TSN or inc./coh ratios. Elevated Zr in organic-rich Unit 6 is a matrix effect (Figure S5). The scanning location of cryptotephra deposits was confirmed by pollen counting. S is a fine-grained Sr-rich minerogenic outwash sand layer. Correlation and PCA analysis plots shown in this diagram are summarised in (B)–(H) overpage.

LP08 200 µm & 2mm (Elements/inc.+coh. as %TSN; log_n transformed)

**B PC 1–9 Scree plot
(standardised, centred)**



**C Correlation matrix of key elements
>0.1% mean, >0.5% max.**

	coh/inc	inc/coh	-1												
coh	0.79	-0.77													
inc	0.94	0.95	-0.94												
Zr	0.75	0.85	0.59	-0.57											
Sr	-0.21	-0.64	-0.42	-0.77	0.76										
Rb	-0.63	-0.62	-0.92	-0.81	-0.92	0.92									
Br	-0.81	-0.56	0.49	0.8	0.67	0.83	-0.83								
Zn	-0.77	0.88	0.56	-0.58	-0.87	-0.76	-0.87	0.87							
Fe	0.82	-0.74	0.89	0.64	-0.73	-0.95	-0.9	-0.91	0.89						
Mn	0.36	0.15	-0.11	0.17	0.24	-0.46	-0.4	-0.49	-0.28	0.26					
Ti	0.16	0.86	0.82	-0.8	0.87	0.8	-0.47	-0.87	-0.69	-0.94	0.94				
Ca	0.38	0.57	0.37	0.16	-0.15	0.21	0.59	-0.19	-0.35	-0.28	-0.37	0.36			
K	0.19	0.88	0.18	0.91	0.91	-0.83	0.95	0.6	-0.67	-0.95	-0.85	-0.94	0.93		
S	-0.44	0.29	-0.43	0.03	-0.37	-0.42	0.41	-0.43	-0.24	0.24	0.4	0.35	0.4	-0.41	
Si	-0.33	0.76	0.34	0.86	0.1	0.71	0.72	-0.7	0.75	0.72	-0.35	-0.74	-0.55	-0.82	0.83

**D PC1–4 Loadings Plots
(standardised, centred)**

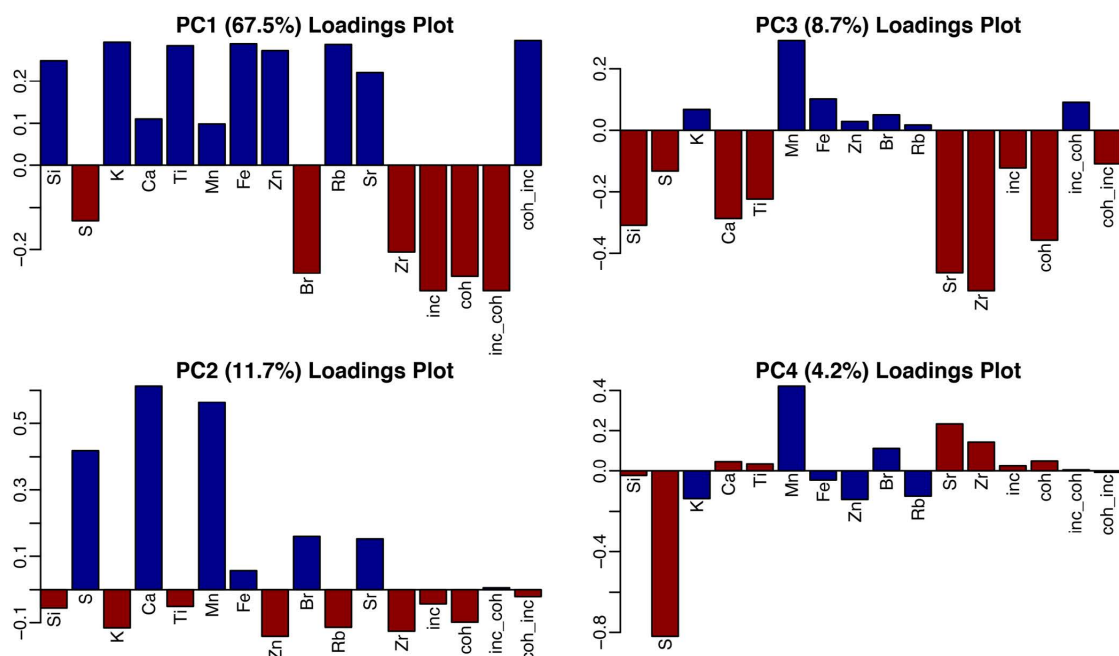
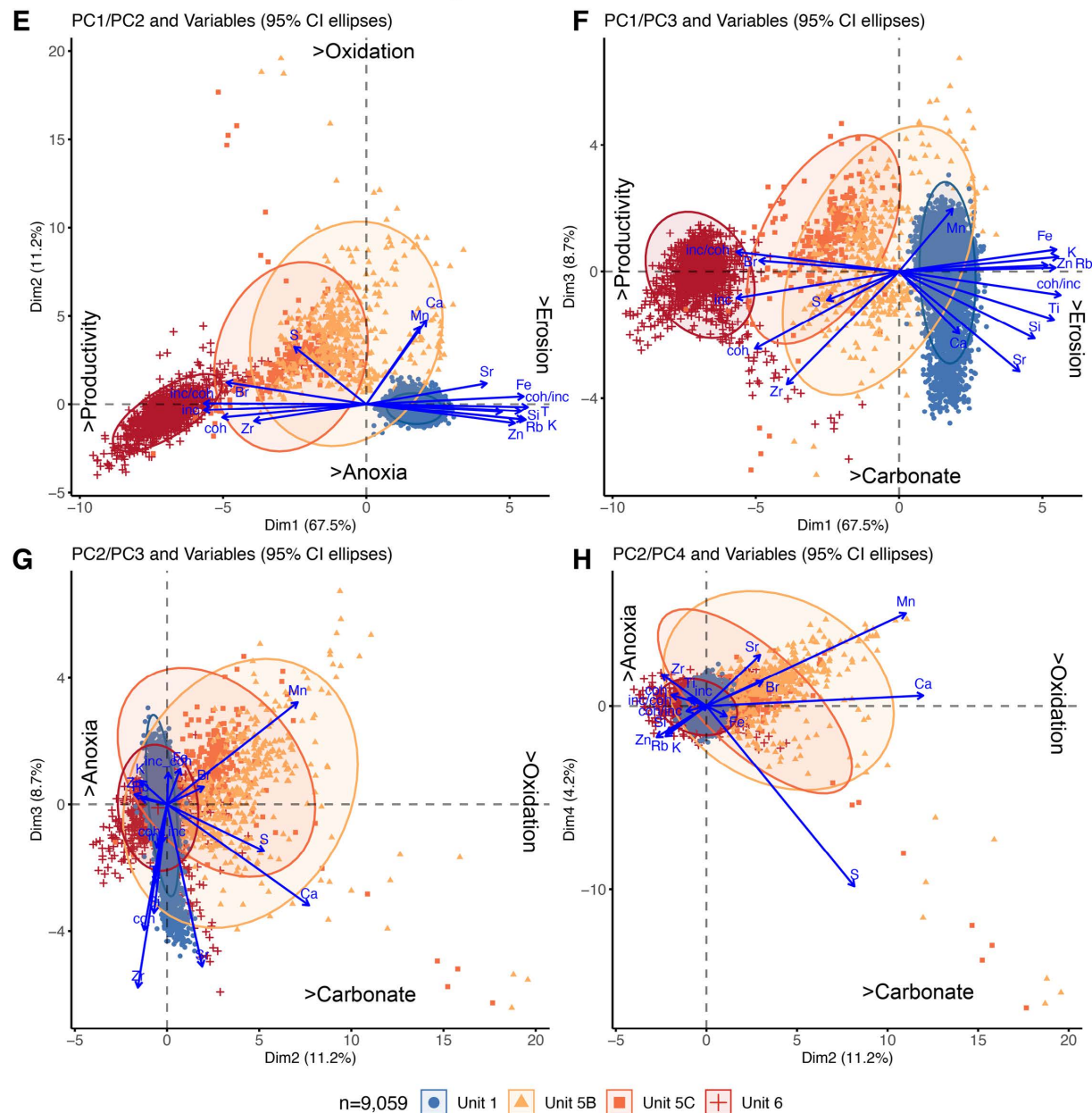


Figure S2. (B) Scree plot summarizing the percentage of variance explained by PC dimensions PC1–9. **(C)** Correlation matrix for key elements and scatter parameters and ratios present in

the LP08 200 μm –2 mm dataset ($n = 9,059$). Key elements were defined as having a mean $>0.1\%$ TSN value and a maximum TSN value of 0.5% or greater. **(D)** Loadings plots for PC1–4 summarising positive and negative element groups. **(E–H) below:** PC1–4 biplot combinations and summary interpretation of each axis for the LP08 200 μm –2 mm dataset, grouped by unit, as defined by CONISS cluster analysis, shown in (A). Data were log_n transformed, centred, and standardised (Z-scores) for PCA analysis. Data and code can be found at: https://github.com/stever60/Lago_Pato.

LP08 200 μm & 2mm (as measured; log_n transformed, standardised, centred)



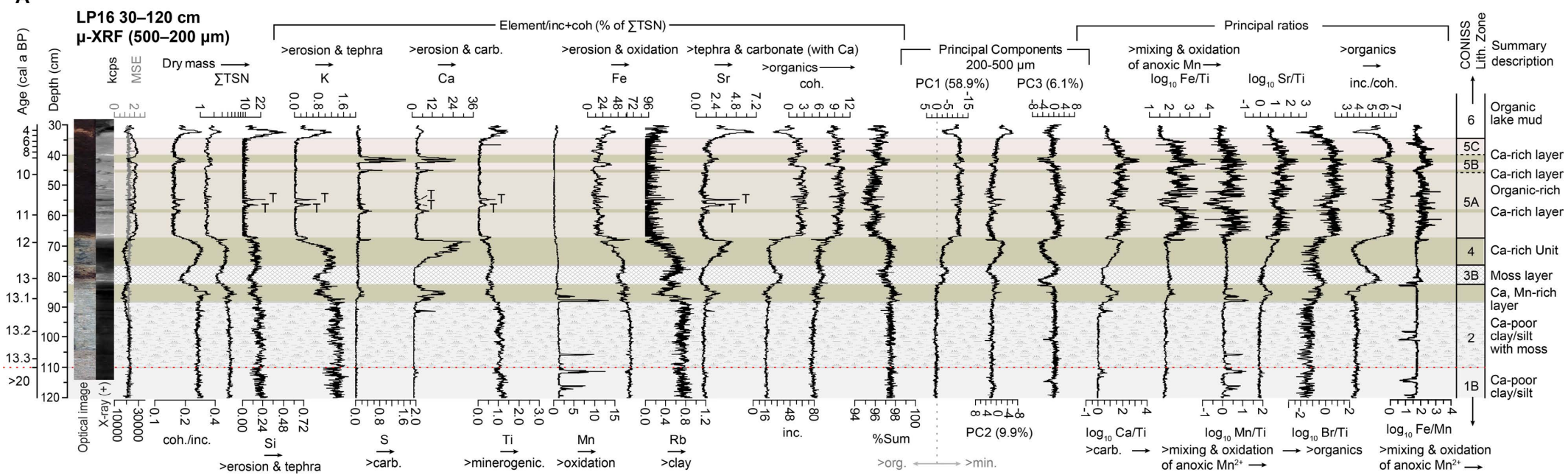
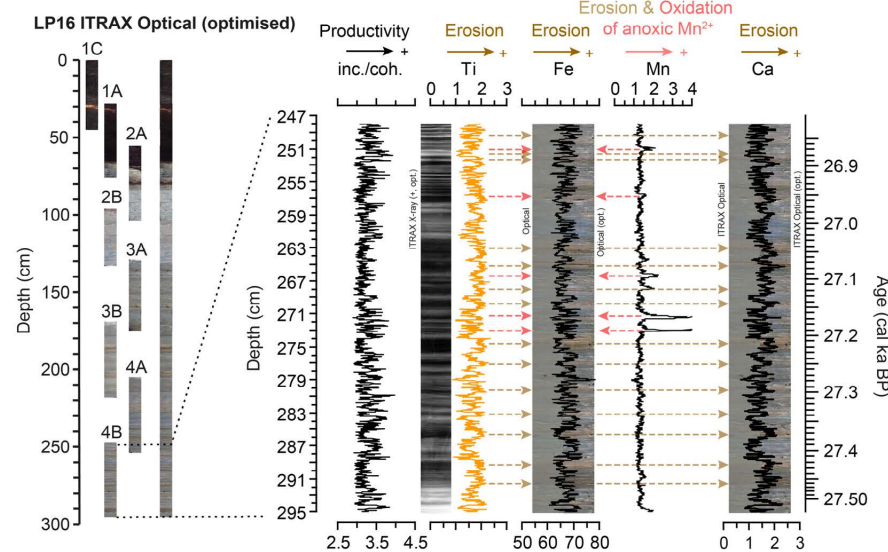
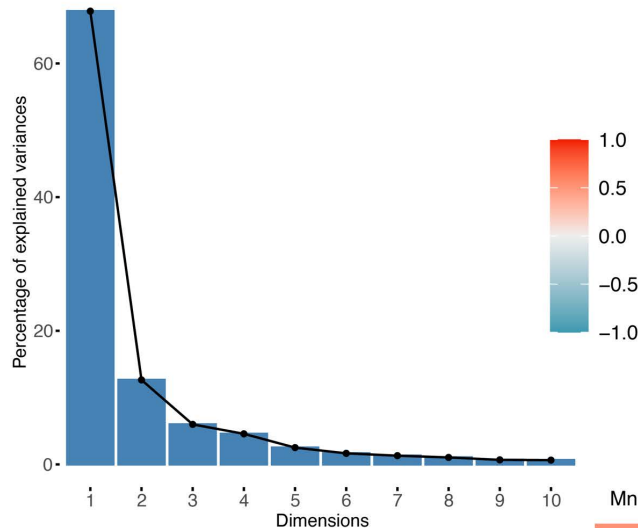
A**B**

Figure S3. (A) Detailed μ -XRF scanning parameters for the Late-glacial–Holocene transitional sediments in the LP16 record, showing erosional (Ti and Fe as % of TSN), oxidation (Mn, Mn/Ti, Fe/Mn), carbonate (S, Ca/Ti) and organic (Br, inc./coh.) proxies. As for LP08, Br is positively correlated with inc./coh. scatter ratio due to vegetational sequestration (aquatic and terrestrial). **(B)** Blow up of the basal LP16 core section showing similar cyclicity in erosional elements as found in the basal Unit 1 of the LP08 record. Figure S6 summarizes time series analysis of Unit 1 in LP16.

Figure S3(C–I): overpage.

LP16 200–500 µm (Elements/inc.+coh. as %TSN; log_n transformed)

**C PC 1–9 Scree plot
(standardised, centred)**



**D Correlation matrix of key elements
>0.1% mean, >0.5% max.**

	coh/inc	inc/coh	coh/coh	inc/coh	coh/coh
coh	-0.99				
inc	0.77	-0.75			
inc	0.96	0.92	-0.9		
Zr	0.81	0.88	0.6	-0.56	
Sr	0.36	0.56	0.04	-0.03	
Rb	-0.29	-0.61	-0.77	-0.71	-0.75
Br	-0.75	0.29	0.64	0.83	0.82
Zn	-0.73	0.85	-0.32	-0.6	-0.75
Fe	0.81	-0.83	0.85	-0.3	-0.75
Mn	0.68	0.46	-0.55	0.47	-0.26
Ti	0.52	0.82	0.72	-0.74	0.74
Ca	-0.46	-0.41	-0.58	-0.53	0.45
K	-0.56	0.83	0.57	0.93	0.88
S	-0.67	0.6	-0.66	-0.51	-0.68
Si	-0.56	0.69	-0.31	0.93	0.44

**E PC1–4 Loadings Plots
(standardised, centred)**

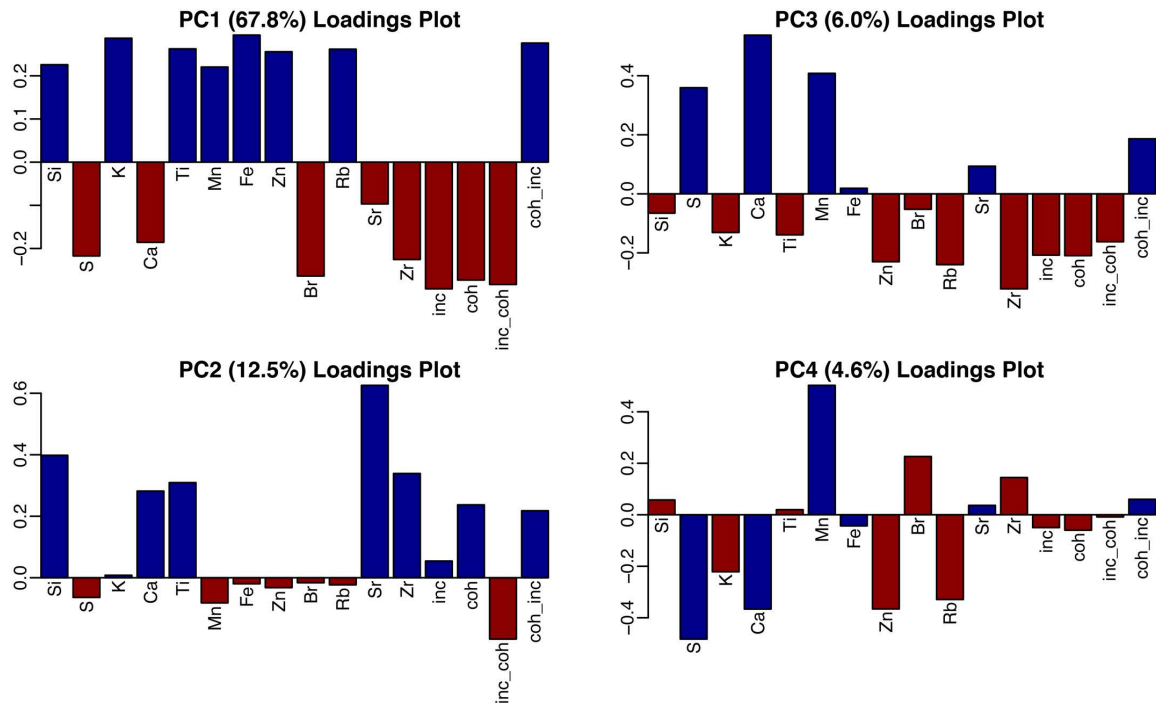
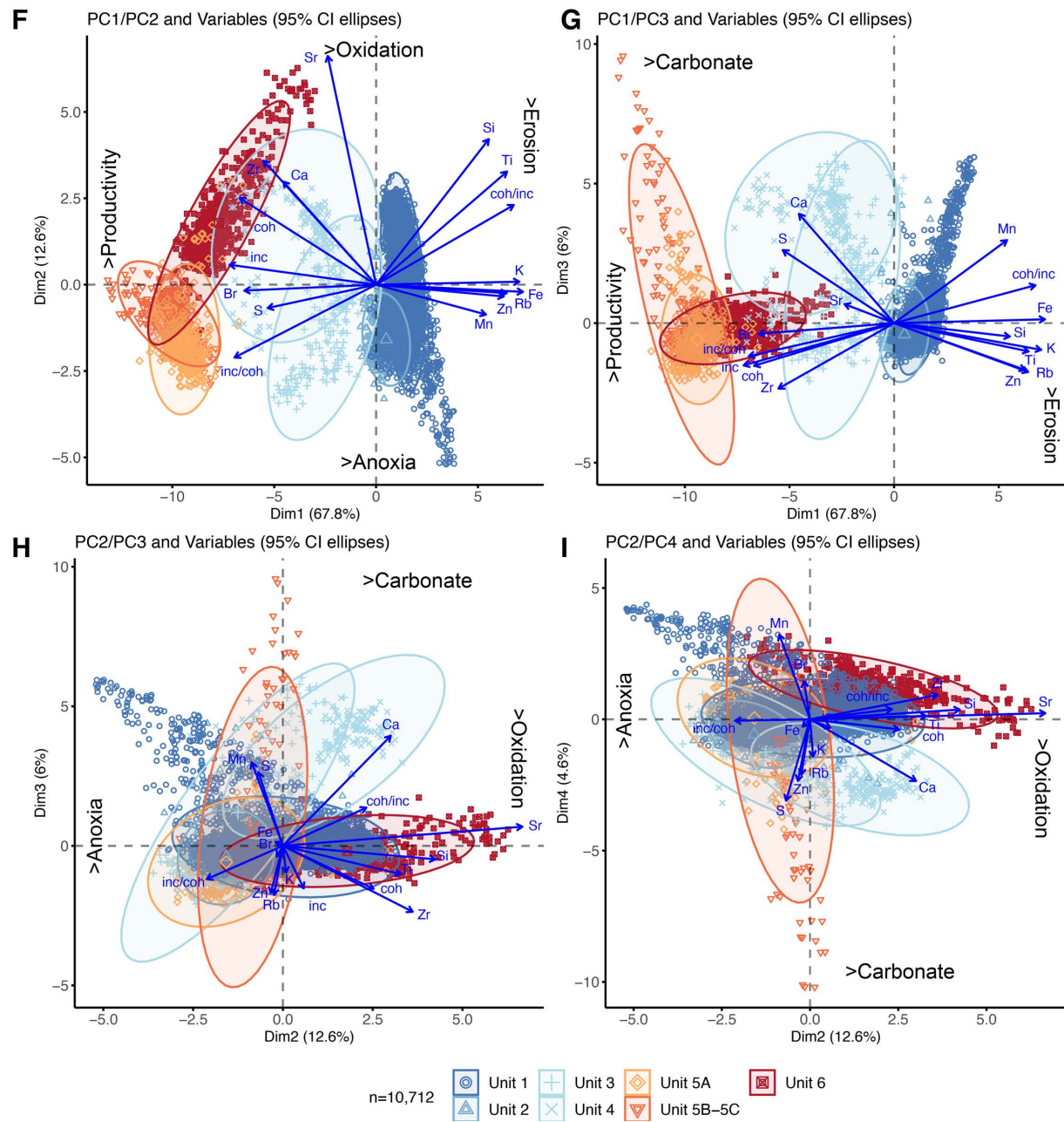


Figure S3. (C) Scree plot summarizing the percentage of variance explained by PC dimensions PC1–9 for the LP16 200–500 µm dataset ($n = 10,712$). (D) Correlation matrix for key elements and scatter parameters and ratios present in the LP16 200–500 µm dataset. Key elements were defined as having a mean >0.1% TSN value and a maximum TSN value of 0.5% or greater. (E)

Loadings plots for PC1–4 summarising positive and negative element groups. (F–I) below PC1–4 biplot combinations and summary interpretation of each axis for the LP16 200–500 μm dataset grouped by unit, as defined by CONISS cluster analysis, shown in (A). Data were log_n transformed, centred, and standardised (Z-scores) for PCA analysis. Data and code can be found at: https://github.com/stever60/Lago_Pato.

LP16 200–500 μm (Elements/inc.+coh. as %TSN; log_n transformed standardised, centred)



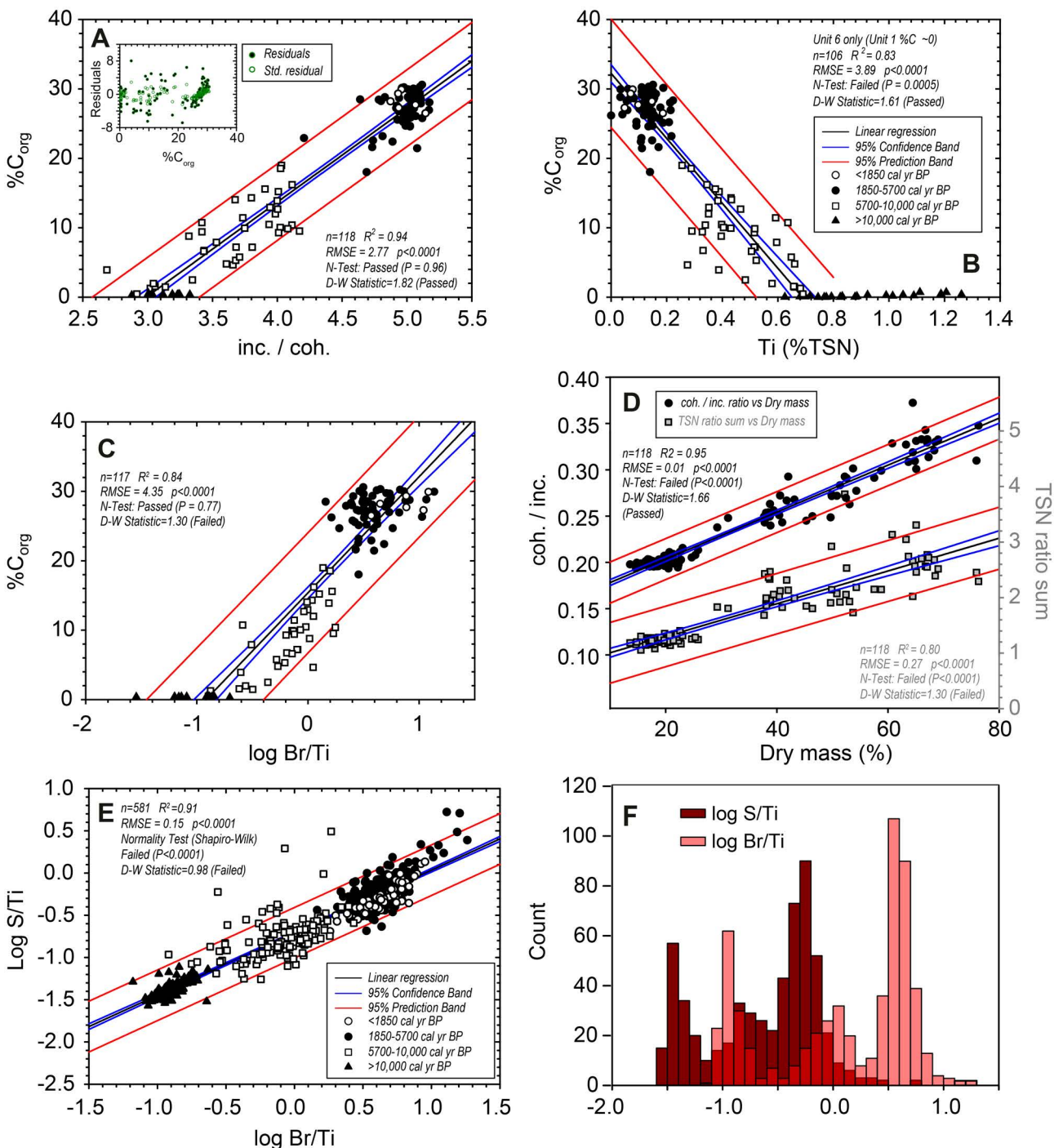


Figure S4. Regression analysis and comparison of key productivity- and erosion-related XRF-CS parameters in the LP08 1 cm dataset. Organic carbon (C_{org}) subsample data are plotted against: (A) inc./coh. scatter ratio. (B) Ti (expressed as % of TSN ratio). (C) Log (Br/Ti). (D) Regression analysis of the TSN ratio (ϕ) and coh. / inc. ratio with subsample dry mass data. (E), (F) Regression analysis of log (S/Ti) against log (Br/Ti) showing the significant correlation between Br and S and histograms showing distinct phases of organic sedimentation with different data distributions and count levels for Br and S enrichment. In summary, these graphs show that three clearly defined organic carbon zones existed at: >c. 10 cal ka BP (Unit 1), between c. 10–5.7 cl ka BP (Unit 5), 5.7–1.9 cal ka BP (Unit 6). The inc./coh. scatter ratio is strongly and significantly correlated to %C_{org} (n = 118; r = 0.96; p<0.0001; R² = 0.94), passing Shapiro-Wilkinson normality and auto-correlation (N-test) tests. Log (Br/Ti) vs %C_{org} (not shown) log (Br/Ti) vs log(S/Ti) (n = 581; r = 0.95; p<0.0001; R² = 0.91) are also strongly and significantly correlated but Br/Ti and S/Ti datasets fail normal distribution tests. Regression analysis involving Br/Ti fails autocorrelation tests. No direct matches between subsample and core scan data were possible for data younger than c. 1.4 cal ka BP. D-W is the Durbin-Watson

Statistic run at 5% significance level to test for autocorrelation in residuals, with zero representing a strong positive serial correlation, four a strong negative serial correlation and two no autocorrelation. For all datasets, n>50, i.e., above the recommended upper sample size limit for N- and D-W tests.

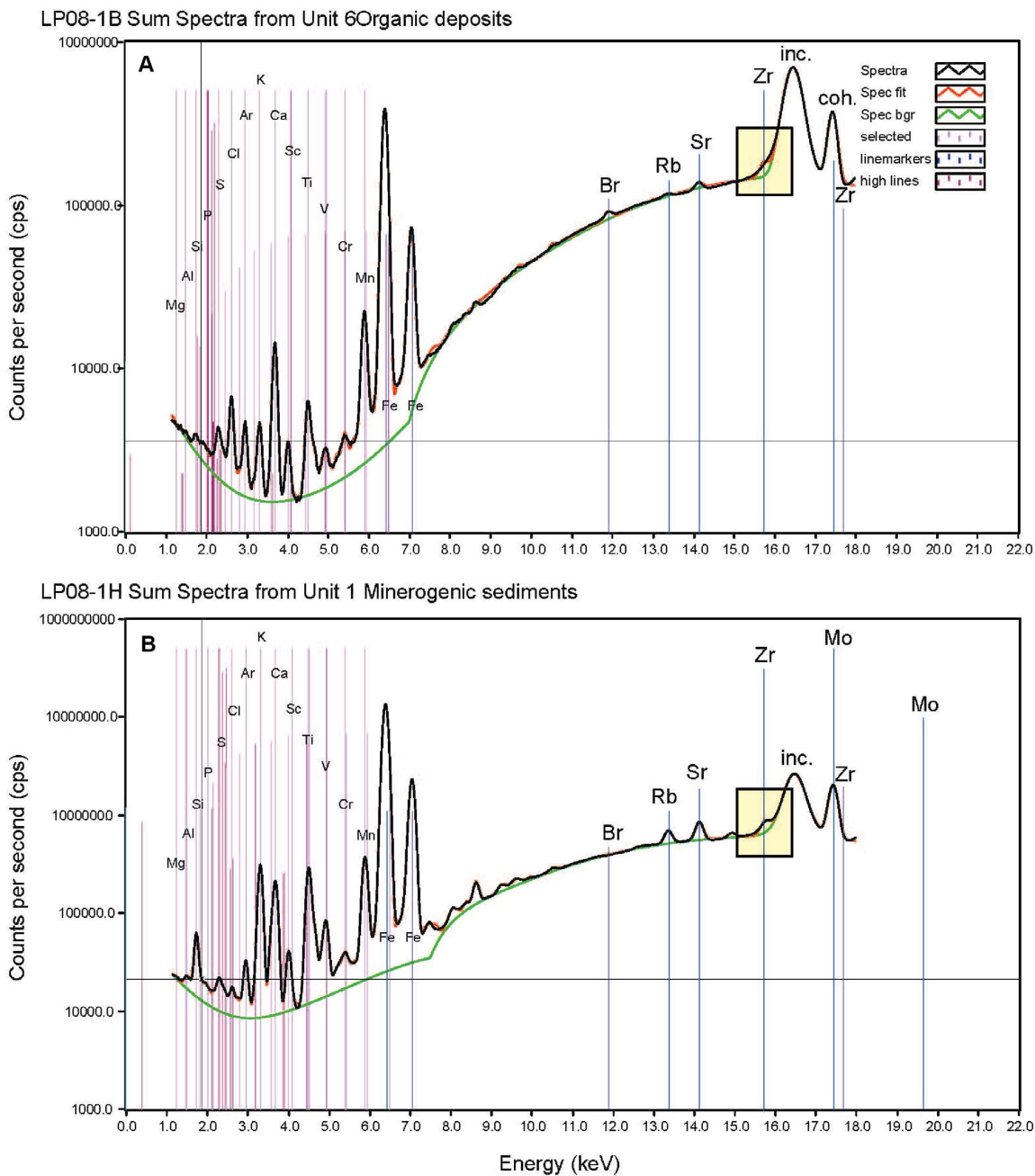


Figure S5. XRF core scanning sumspectra profiles for core **(A)** PAT1B and **(B)** PAT1H showing contrasting spectra obtained organic- and minerogenic-dominated sediment matrices. The spectra mismatch for Zr is due to an organic matrix effect that artificially elevates Zr cps, rendering this element unreliable as a grain size proxy in the upper half of the Lago Pato core.

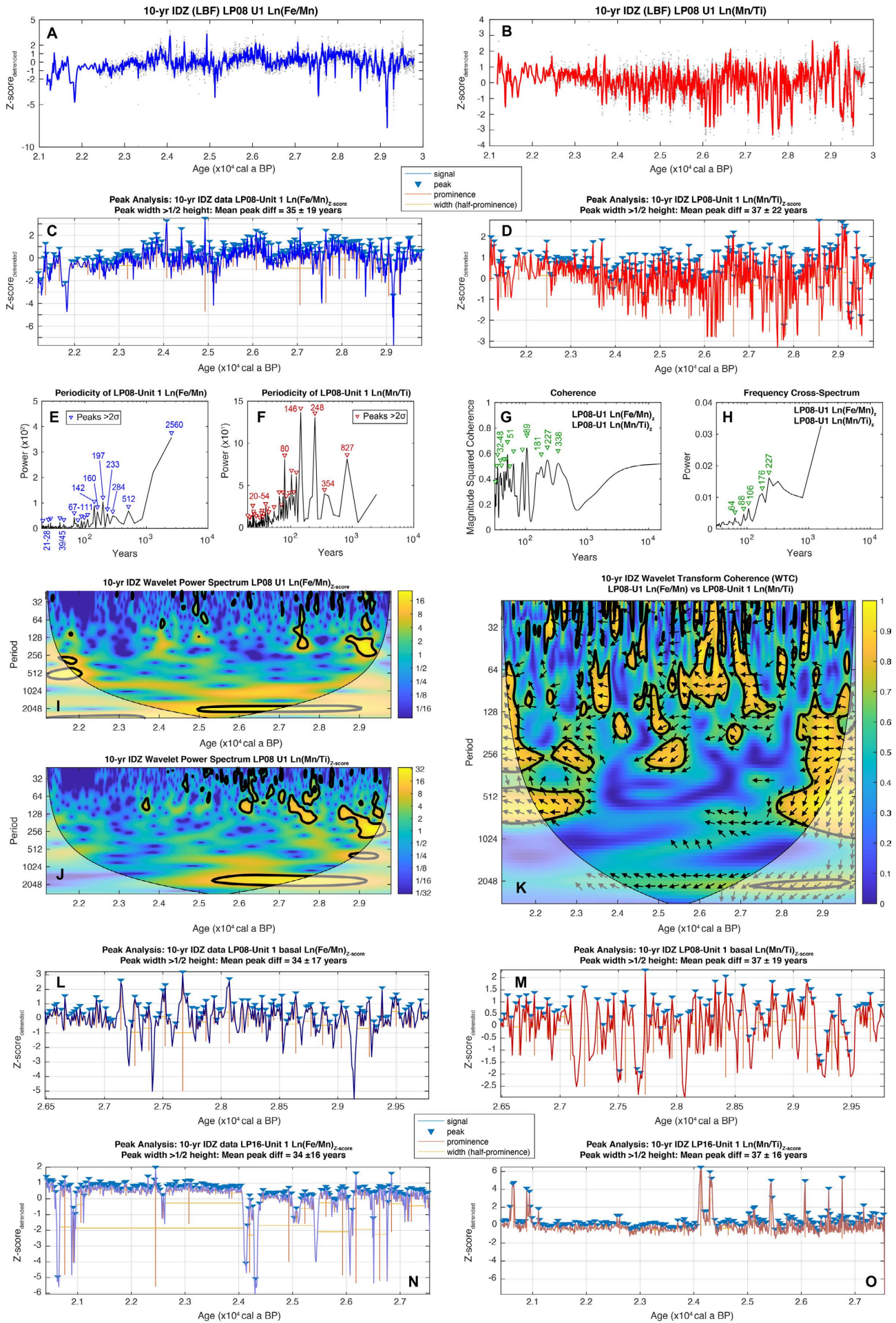


Figure S6. Time series, peak analysis, and wavelet power spectral analysis for the 10-year PCHIP (Piecewise Cubic Hermite Interpolating Polynomial) interpolated datasets from the 200 μm LP08

Unit 1, LP08 Unit 1 basal core section and LP16 Unit datasets **(A)** $\text{Ln(Fe/Mn)}_{\text{Z-scores}}$ (blue line) and **(B)** $\text{Ln(Mn/Ti)}_{\text{Z-scores}}$ (red line) from Unit 1 in the LP08 record. The mean sample interval for the dataset (grey dots) is 1.26 ± 4.23 years. **(C)** Peak identification and interval analysis for $\text{Ln(Fe/Mn)}_{\text{Z-scores}}$ from the LP08 Unit 1 dataset, resulting in a mean peak difference of 35 ± 19 years. Prominent peaks were defined as peak width being greater than half its height. **(D)** Peak identification and interval analysis for the LP08 Unit 1 $\text{Ln(Mn/Ti)}_{\text{Z-scores}}$ dataset resulting in a mean peak difference of 37 ± 22 years. **(E, F)** Power spectrum periodicity for interpolated and detrended LP08 Unit 1 $\text{Ln(Fe/Mn)}_{\text{Z-scores}}$ (blue) and $\text{Ln(Mn/Ti)}_{\text{Z-scores}}$ (red). **(G, H)** Cross-coherence and cross-spectrum bi-plots for interpolated and detrended $\text{Ln(Mn/Ti)}_{\text{Z-scores}}$ and $\text{Ln(Fe/Mn)}_{\text{Z-scores}}$ datasets with prominent centennial scale periodicities highlighted. **(I, J, K)** Wavelet power spectrum and wavelet transform coherence (WTC) plots (Grinsted et al., 2004) showing centennial-scale periodicity and time-dependent changes in cycle correlation between $\text{Ln(Mn/Ti)}_{\text{Z-scores}}$ and $\text{Ln(Fe/Mn)}_{\text{Z-scores}}$ datasets. WTC uses Monte Carlo methods to assess the statistical significance of cross-coherence against red noise in both time series. Significant ($>95\%$ confidence) decadal–centennial scale periodicities and correlations are outlined in black. **(L)** Peak identification and interval analysis for $\text{Ln(Fe/Mn)}_{\text{Z-scores}}$ from the LP08 Unit 1 basal core section dataset shown in Figure 6C–F, resulting in a mean peak difference of 34 ± 17 years. Prominent peaks were defined as peak width being greater than half its height. **(M)** Peak identification and interval analysis for $\text{Ln(Mn/Ti)}_{\text{Z-scores}}$ from the LP08 Unit 1 basal core section dataset shown in Figure 6C–F, resulting in a mean peak difference of 37 ± 19 years. **(N)** Peak identification and interval analysis for $\text{Ln(Fe/Mn)}_{\text{Z-scores}}$ from the LP016 Unit 1 dataset, resulting in a mean peak difference of 34 ± 16 years. Prominent peaks were defined as peak width being greater than half its height. **(O)** Peak identification and interval analysis for $\text{Ln(Mn/Ti)}_{\text{Z-scores}}$ from the LP08 Unit 1 basal core section dataset shown in Figure 6C–F, resulting in a mean peak difference of 37 ± 15 years. Data and code can be found at: https://github.com/stever60/Lago_Pato.

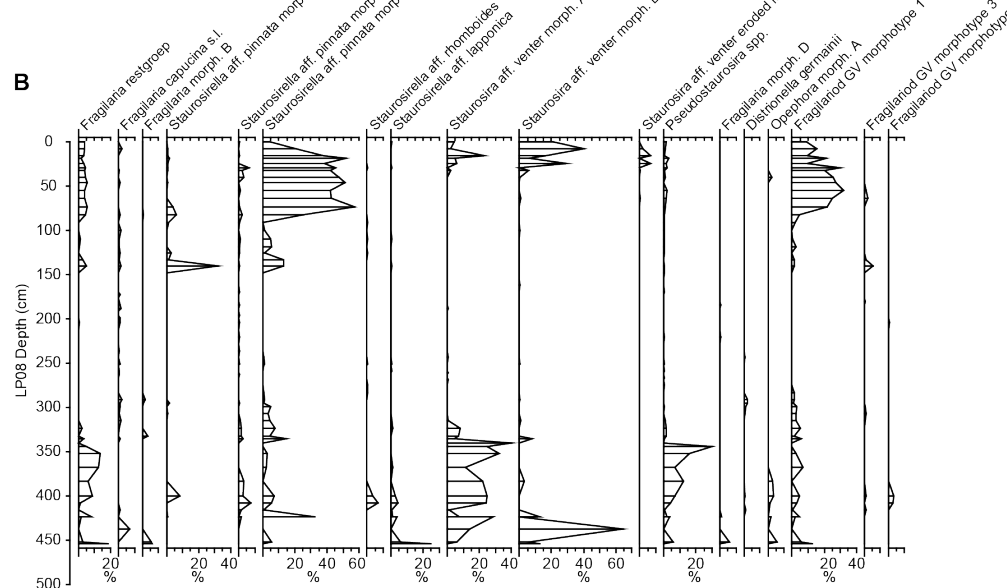
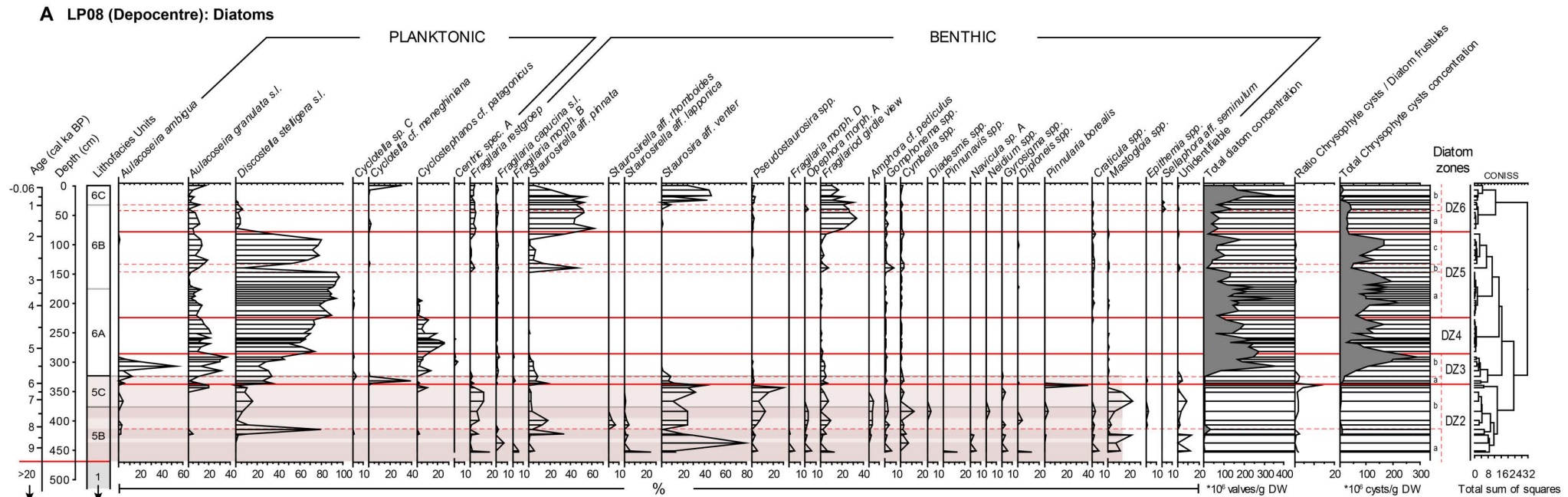
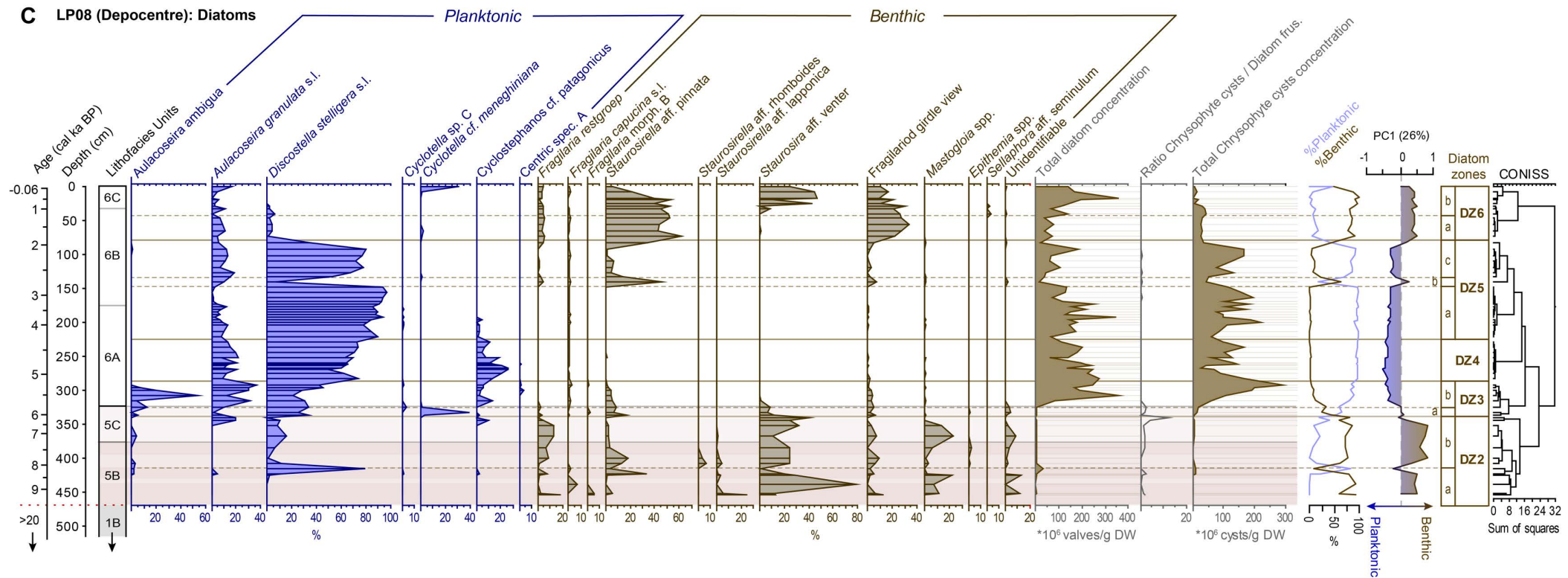


Figure S7. (A) Full diatom percentage count data for the LP08 record. (B) Fragilariod diatom species profile from the LP08 record. (C) Overpage: Summary diatom species composition diagram for Holocene-age sediments in the LP08 record. CONISS with broken stick analysis was used to define the statistically significant diatom zones DZ1-DZ6. Insufficient diatoms for counting statistics were present in the pre-Holocene age sediments in the LP08 record. PCA axis 1 diatom data represent major shifts between planktonic (0–1) and benthic species (0– -1), representing deeper (wetter) and more stable conditions versus shallower (drier) more turbulent conditions.

C LP08 (Depocentre): Diatoms



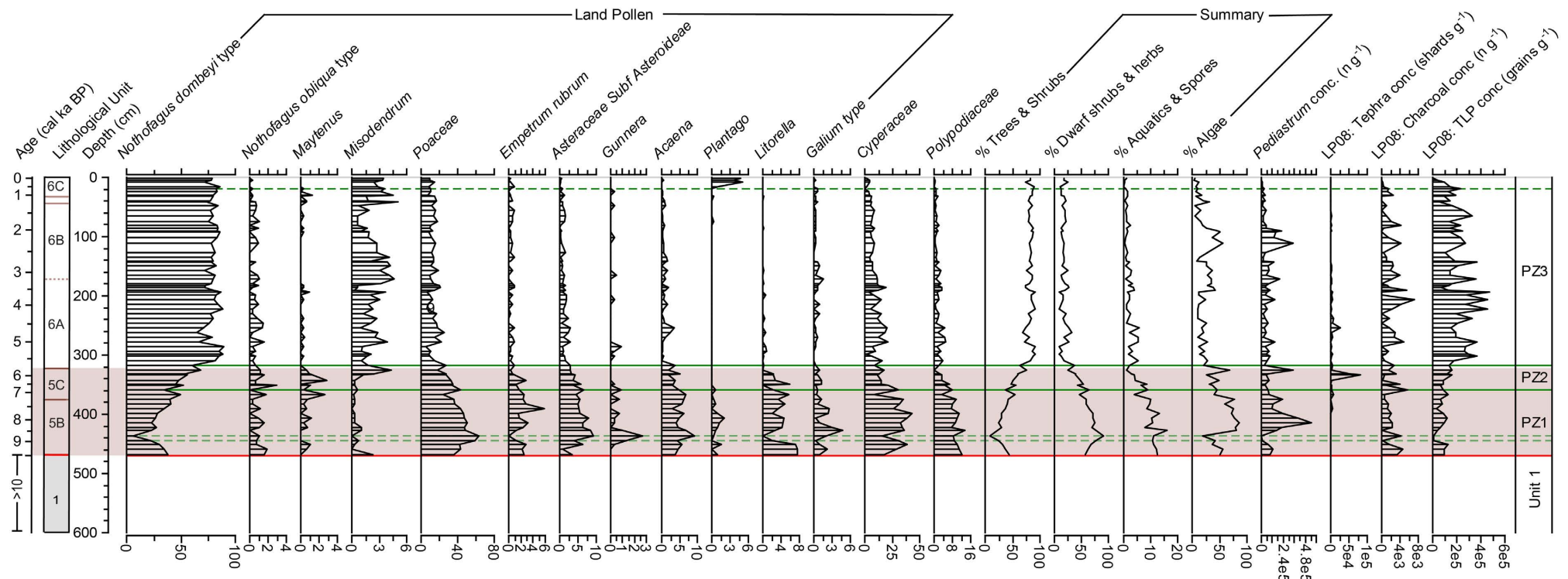


Figure S8. Full pollen count data for the LP08 record.

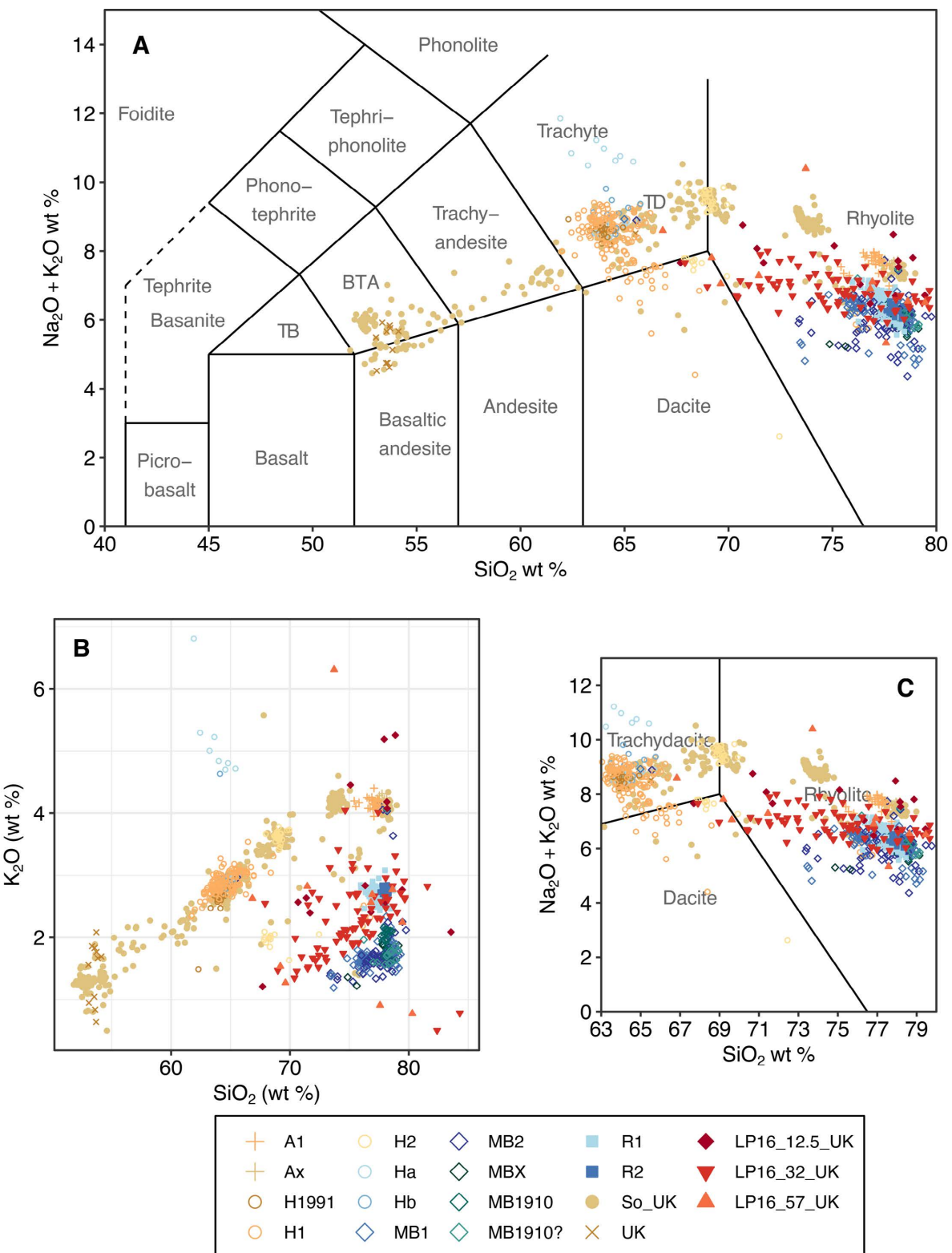


Figure S9. (A) Total Alkali Silica (TAS) (Le Bas et al., 1986) and **(B)** $\text{K}_2\text{O}/\text{SiO}_2$ biplots used to classify and assess potential correlatives for Lago Pato (LP) volcanic glass shard EPMA data ($n_{\text{unfiltered}} = 1138$; $n_{\text{filtered}} = 1119$; $n_{\text{ACID}} = 967$; $n_{\text{RHY}} = 644$; Supplementary Dataset) compared to key eruptions from the Southern South America volcanoes: A = Aguillera, H = Hudson, MB = Mount Burney, R = Reclus, So = Solipuli; UK = Unknown. TB is Trachybaset TBA is Basalt-trachy-andesite. Data were filtered to remove totals <97% (<63% SiO_2) <95% (>63% SiO_2) and normalised to 100% on a water-free ($\text{H}_2\text{O}_{\text{TOTAL}}$) basis. **(C)** Zoom in of (A).

Figure S9. (D–G) Overpage.

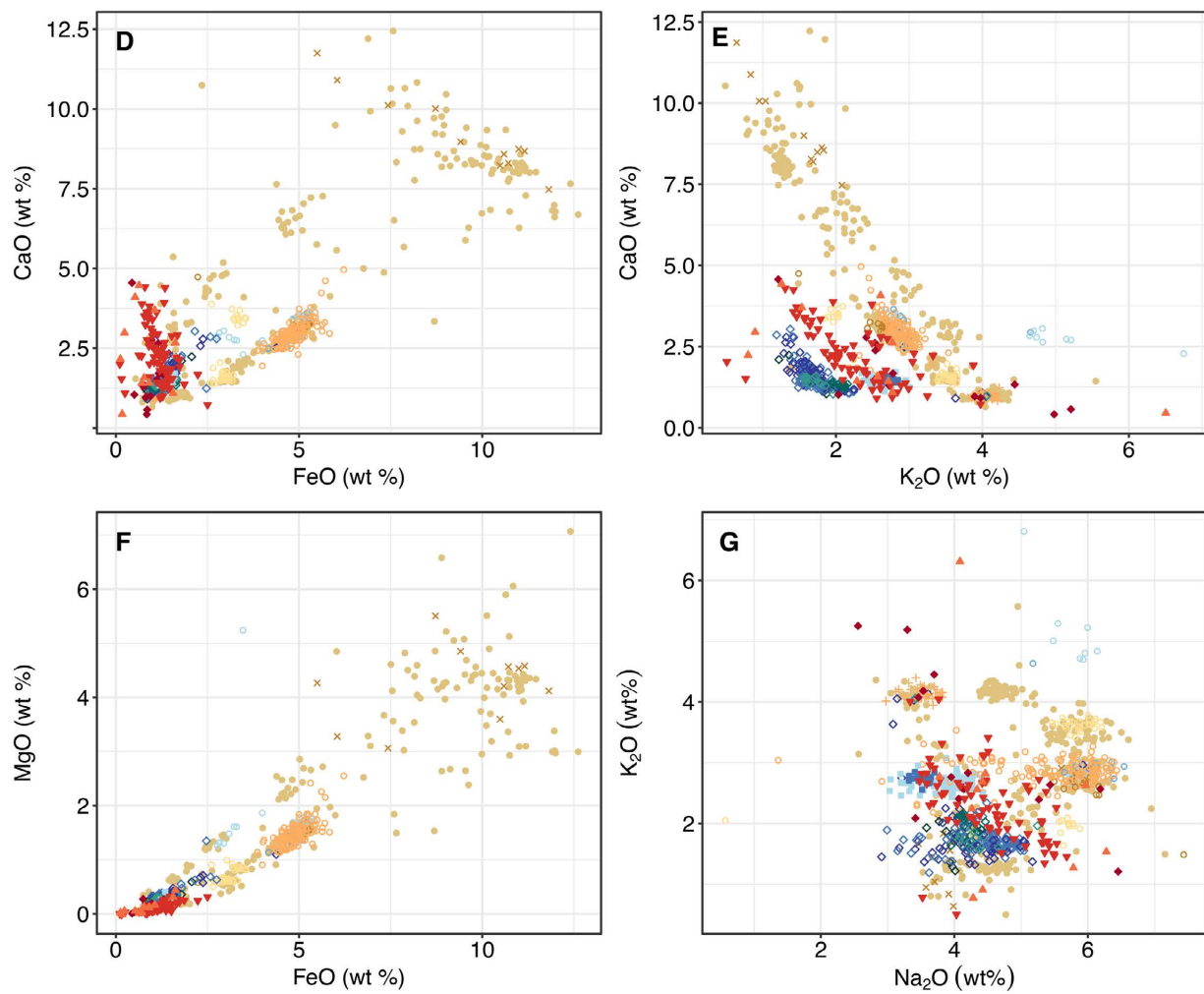
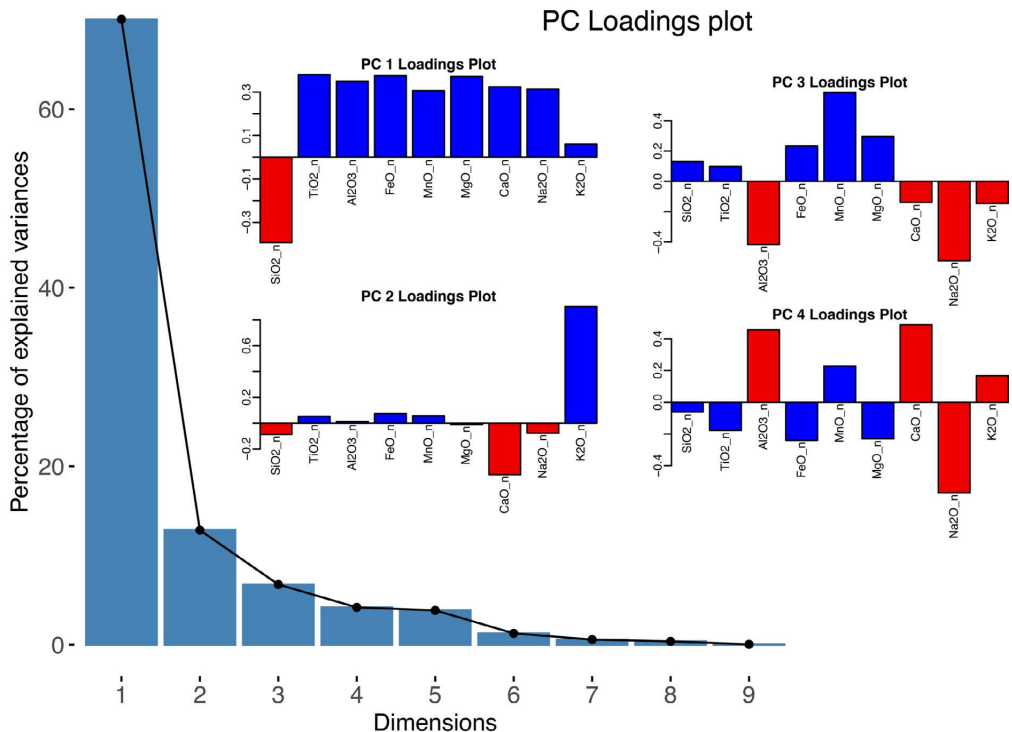


Figure S9 contd. Elemental biplots used to assess potential correlatives for the Lago Pato tephra EPMA shard data (Table S2) **(D)** CaO/FeO; **(E)** CaO/K₂O; **(F)** Na₂O/ K₂O; **(G)** FeO/TiO₂. Reference data and references can be found at: https://github.com/stever60/Lago_Pato

A Scree plot



B PC2/PC3 and Variables (68% CI)

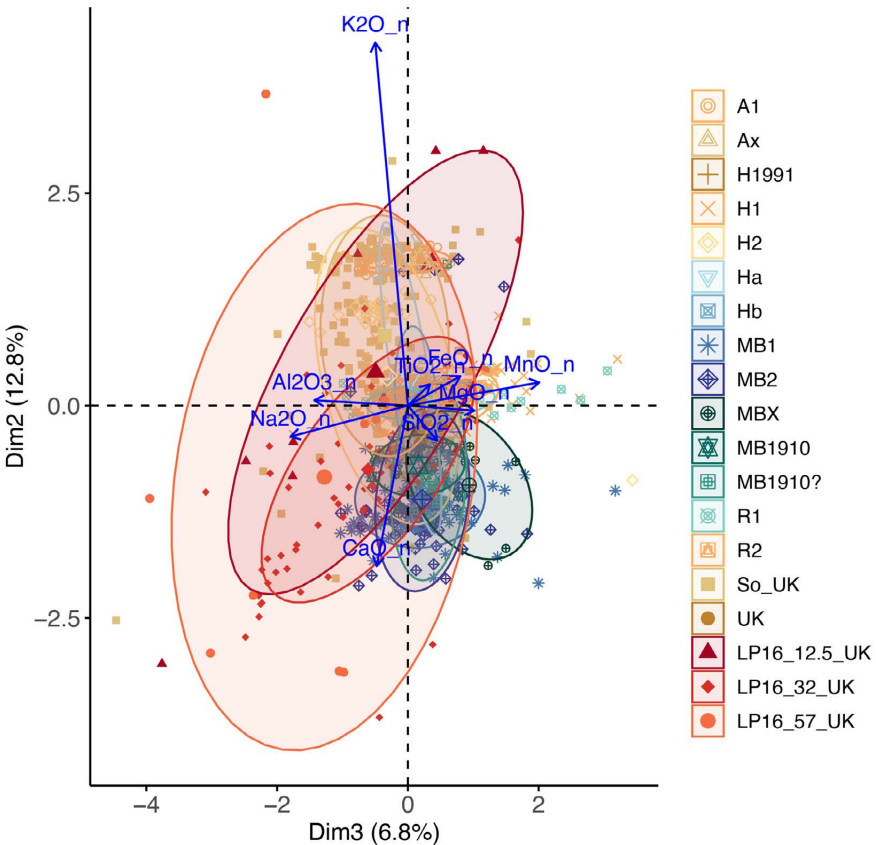


Figure S10. Principal components analysis of data showing: (A) Scree plot of variance explained by PC dimensions (axes) 1–9 and PC1–4 loadings. (B) PC2/ PC4 biplot of rhyolitic glass shards from Lago Pato (LP) volcanic glass shard EPMA data ($n_{\text{unfiltered}} = 1,138$; $n_{\text{filtered}} = 1,119$; $n_{\text{ACID}} = 967$; $n_{\text{RHY}} = 644$; Supplementary Dataset) compared to key eruptions from the Southern South America volcanoes: A = Aguillera, H = Hudson, MB = Mount Burney, R = Reclus, So = Solipuli; UK = Unknown. Data were filtered to remove totals <95%, normalised to 100%, square root transformed, and standardised and centered.

4. Supplementary Tables

Table S1 Correlation table and figure matrix comparing r^2 values, bi-plots and density distributions of 1 cm resolution, 4 cm interval subsample data and 1 cm resolution matched XRF-CS data for the LP08 record. GRD = GEOTEK-MSCL wet Gamma Ray Density; DW = Dry Weight; TOC_N = Total Organic Carbon undertaken at NIGL; LOI950_c = Loss on Ignition at 950 °C x 1.36 carbonate proxy; % of Total Scatter Normalised Ratio Sum (%TSN) for Ti, Br, and Ca; inc_coh = inc./coh ratio; coh_inc = coh./inc. ratio; TSN_RS = Total Scatter Normalised Ratio Sum. Pearson Correlation Coefficients r values: Corr = whole record; U1 = Unit1 (red), U5 = Unit 5 (green), and U6 (blue) = Unit 6; Significance test: *** p<0.0001; ** p<0.001; * p<0.05; . p<0.1; no symbol p>0.1.

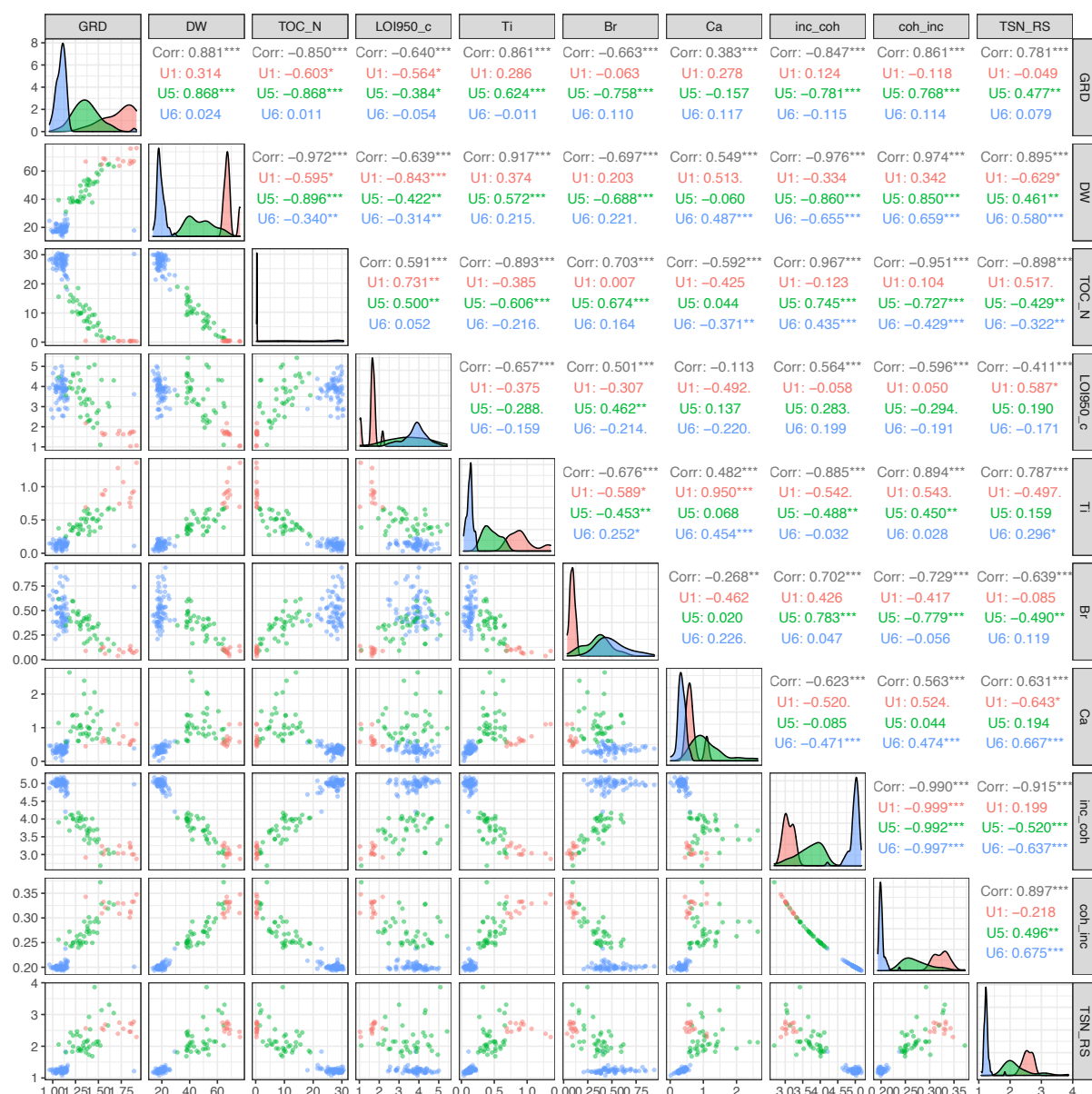


Table S2 Glass shard cryptotephra EPMA data for the Lago Pato LP16 record.

Lab ID	Size μm	Na ₂ O	Al ₂ O ₃	MgO	SiO ₂	K ₂ O	CaO	FeO	P ₂ O ₅	TiO ₂	MnO	Total
LP16_12.45	63-125	3.36	11.40	0.14	74.28	3.98	0.92	0.78	0.02	0.13	0.03	95.05
LP16_12.45	63-125	3.31	11.46	0.14	74.72	3.89	0.96	0.90	0.02	0.14	0.02	95.58
LP16_12.45	63-125	3.16	11.53	0.06	74.79	4.98	0.41	0.81	0.05	0.14	0.03	95.98
LP16_12.45	63-125	3.69	14.34	0.06	74.92	4.44	1.33	0.79	0.04	0.15	0.03	99.78
LP16_12.45	63-125	4.09	13.24	0.27	77.18	2.42	1.68	1.31	0.06	0.20	0.04	100.48
LP16_12.45	63-125	2.54	11.23	0.09	78.22	5.21	0.57	0.85	0.06	0.39	0.03	99.18
LP16_12.45	63-125	5.31	16.50	0.20	72.34	2.42	2.78	0.98	0.13	0.21	0.04	100.91
LP16_12.45	125-250	4.10	12.04	0.11	77.21	2.54	1.50	1.10	0.07	0.24	0.04	98.94
LP16_12.45	125-250	6.48	19.48	0.01	67.96	1.21	4.57	0.44	0.06	0.17	0.02	100.39
LP16_12.45	125-250	3.90	11.05	0.27	78.48	2.73	1.29	0.74	0.06	0.22	0.04	98.78
LP16_12.45	125-250	3.33	8.89	0.03	81.44	2.03	1.02	0.49	0.09	0.16	0.00	97.48
LP16_12.45	125-250	5.24	15.94	0.11	68.77	2.54	2.38	1.02	0.11	0.20	0.06	96.36
LP16_12.45	125-250	4.12	13.08	0.10	74.85	2.78	1.68	1.16	0.09	0.18	0.03	98.06
LP16_12.45	125-250	4.82	15.81	0.09	63.19	2.14	3.30	0.76	0.08	0.14	0.03	90.34
LP16_12.45	125-250	6.10	16.22	0.08	69.71	2.53	2.61	1.14	0.06	0.13	0.03	98.63
LP16_32.2	63-125	3.38	11.12	0.07	71.95	2.90	0.96	0.73	0.07	0.18	0.03	91.37
LP16_32.2	63-125	4.39	14.44	0.03	72.18	3.33	2.22	0.61	0.05	0.18	0.02	97.46
LP16_32.2	63-125	5.48	15.23	0.09	72.36	2.24	2.55	0.89	0.05	0.19	0.03	99.11
LP16_32.2	63-125	3.64	10.54	0.08	76.17	2.61	1.21	1.41	0.08	0.25	0.05	96.03
LP16_32.2	63-125	3.46	9.35	0.01	82.67	0.77	1.51	0.15	0.05	0.13	0.00	98.08
LP16_32.2	63-125	3.92	12.50	0.04	74.92	2.24	2.18	0.68	0.07	0.29	0.04	96.87
LP16_32.2	63-125	5.20	16.86	0.05	68.33	1.31	4.29	0.77	0.05	0.22	0.02	97.09
LP16_32.2	63-125	4.90	14.90	0.15	70.73	1.57	3.34	0.88	0.06	0.20	0.05	96.79
LP16_32.2	63-125	4.09	10.53	0.08	77.20	2.56	0.91	1.17	0.07	0.27	0.04	96.91
LP16_32.2	63-125	5.33	16.85	0.06	70.89	1.69	3.62	1.11	0.07	0.23	0.04	99.88
LP16_32.2	63-125	3.67	11.45	0.05	75.23	2.38	1.79	1.46	0.05	0.24	0.03	96.36
LP16_32.2	63-125	3.61	13.65	0.05	71.56	3.88	1.92	0.88	0.06	0.22	0.04	95.87
LP16_32.2	63-125	5.22	16.05	0.00	71.25	2.70	2.74	0.84	0.06	0.21	0.04	99.12
LP16_32.2	63-125	4.45	13.86	0.32	74.72	2.68	1.77	1.48	0.05	0.20	0.05	99.59
LP16_32.2	63-125	3.74	11.03	0.15	77.27	3.25	0.97	1.26	0.06	0.24	0.03	98.00
LP16_32.2	63-125	4.46	14.07	0.05	74.48	3.15	1.59	0.91	0.06	0.18	0.03	98.97
LP16_32.2	125-250	5.15	16.18	0.10	68.79	1.46	3.42	0.82	0.05	0.16	0.02	96.14
LP16_32.2	125-250	3.74	12.74	0.10	73.72	1.98	1.92	1.16	0.07	0.29	0.04	95.76
LP16_32.2	125-250	4.41	12.76	0.13	74.82	2.20	1.65	1.37	0.07	0.28	0.03	97.72
LP16_32.2	125-250	4.60	14.09	0.14	74.38	1.85	2.34	1.09	0.04	0.25	0.02	98.80
LP16_32.2	125-250	3.68	11.63	0.25	78.24	2.33	1.37	1.86	0.06	0.27	0.04	99.74
LP16_32.2	125-250	4.74	13.27	0.22	72.18	1.69	2.83	1.63	0.05	0.26	0.05	96.91
LP16_32.2	125-250	4.39	13.28	0.09	75.21	2.20	2.20	1.20	0.06	0.27	0.04	98.94
LP16_32.2	125-250	4.08	11.55	0.12	78.17	2.61	1.47	1.44	0.07	0.33	0.03	99.88
LP16_32.2	125-250	4.32	12.23	0.14	75.35	2.60	1.37	1.26	0.08	0.34	0.04	97.71
LP16_32.2	125-250	4.66	16.31	0.08	71.79	1.50	3.60	0.83	0.06	0.28	0.03	99.15
LP16_32.2	125-250	4.45	15.15	0.07	72.73	1.91	2.84	0.98	0.05	0.21	0.02	98.41
LP16_32.2	125-250	4.02	10.85	0.19	76.49	2.33	1.30	1.25	0.06	0.25	0.06	96.80
LP16_32.2	125-250	3.37	12.82	0.18	73.21	2.61	2.79	1.48	0.08	0.29	0.03	96.87
LP16_32.2	125-250	3.31	11.10	0.31	76.74	3.98	0.72	2.48	0.08	0.32	0.07	99.12
LP16_32.2	125-250	4.22	14.13	0.10	72.96	1.95	2.62	1.30	0.06	0.22	0.04	97.59
LP16_32.2	125-250	4.72	12.61	0.11	74.63	2.28	1.82	1.40	0.06	0.22	0.05	97.88
LP16_32.2	125-250	3.73	11.03	0.06	76.12	2.42	1.67	1.32	0.07	0.26	0.04	96.71
LP16_32.2	125-250	4.77	13.47	0.17	75.43	1.91	2.15	1.31	0.06	0.25	0.04	99.56
LP16_32.2	125-250	5.02	14.38	0.22	75.05	2.04	2.16	1.75	0.07	0.27	0.04	101.01
LP16_32.2	125-250	5.00	19.14	0.06	66.43	2.49	3.80	0.69	0.05	0.14	0.02	97.82
LP16_32.2	125-250	3.53	10.69	0.03	82.04	2.84	1.10	0.25	0.02	0.06	0.02	100.58
LP16_32.2	125-250	5.18	14.02	0.09	72.47	1.99	2.47	1.04	0.11	0.28	0.05	97.69
LP16_32.2	125-250	5.18	15.07	0.07	71.00	1.76	3.04	0.93	0.07	0.20	0.03	97.34
LP16_32	63-125	4.11	12.52	0.08	74.22	2.38	1.74	1.16	0.07	0.26	0.03	96.57
LP16_32	63-125	5.18	15.33	0.01	71.16	1.64	3.16	0.79	0.07	0.17	0.01	97.52
LP16_32	63-125	4.44	12.71	0.21	72.69	2.18	1.81	1.23	0.07	0.24	0.04	95.62
LP16_32	63-125	4.47	13.00	0.26	72.98	2.08	1.86	1.68	0.08	0.24	0.03	96.67
LP16_32	63-125	5.32	17.27	0.17	66.73	1.42	4.25	1.30	0.06	0.20	0.03	96.74
LP16_32	63-125	3.55	11.87	0.13	76.18	2.89	1.31	1.29	0.06	0.27	0.05	97.60

LP16_32	63-125	3.49	10.95	0.12	75.94	2.95	1.38	1.08	0.04	0.22	0.03	96.20
LP16_32	63-125	4.37	14.93	0.06	72.06	3.07	2.29	1.12	0.06	0.25	0.03	98.24
LP16_32	63-125	4.56	14.67	0.10	73.01	2.04	2.23	1.24	0.08	0.26	0.04	98.22
LP16_32	63-125	5.54	16.84	0.07	68.76	1.42	3.57	0.92	0.06	0.21	0.04	97.44
LP16_32	63-125	4.36	13.67	0.10	72.42	1.84	2.34	1.13	0.06	0.26	0.03	96.22
LP16_32	63-125	3.53	11.97	0.08	76.83	2.62	1.53	1.52	0.09	0.27	0.05	98.48
LP16_32	63-125	3.49	11.80	0.10	74.72	2.21	2.25	1.34	0.07	0.24	0.04	96.24
LP16_32	63-125	4.09	11.06	0.00	83.51	0.51	2.03	0.11	0.02	0.06	0.02	101.37
LP16_32	63-125	3.89	12.81	0.13	73.97	1.95	2.25	1.13	0.07	0.22	0.01	96.42
LP16_32	63-125	4.95	14.17	0.08	69.49	2.12	2.49	0.88	0.04	0.13	0.02	94.37
LP16_32	63-125	5.19	15.72	0.04	69.14	2.44	2.92	0.96	0.05	0.15	0.03	96.66
LP16_32	63-125	4.25	12.38	0.12	73.48	2.99	1.20	1.21	0.08	0.22	0.03	95.97
LP16_32	63-125	4.36	13.14	0.09	74.01	2.65	1.67	1.37	0.07	0.32	0.04	97.73
LP16_32	125-250	5.35	15.96	0.06	69.71	1.46	3.72	0.90	0.07	0.27	0.02	97.51
LP16_32	125-250	4.10	11.93	0.10	75.89	2.52	1.42	1.33	0.07	0.29	0.05	97.70
LP16_32	125-250	4.37	14.77	0.11	74.42	2.12	2.44	1.19	0.07	0.24	0.06	99.78
LP16_32	125-250	4.99	15.81	0.08	70.73	1.79	3.34	0.87	0.04	0.14	0.02	97.81
LP16_32	125-250	4.39	13.68	0.08	74.97	2.41	2.03	1.12	0.06	0.26	0.04	99.04
LP16_32	125-250	3.48	11.40	0.17	76.33	2.75	1.31	1.30	0.07	0.24	0.02	97.07
LP16_32	125-250	4.64	14.10	0.19	73.84	2.10	1.48	1.38	0.06	0.25	0.05	98.09
LP16_32	125-250	4.08	12.26	0.18	72.90	2.00	2.11	1.58	0.06	0.26	0.04	95.46
LP16_32	125-250	3.52	10.52	0.09	75.80	2.77	0.94	1.19	0.07	0.29	0.04	95.23
LP16_32	125-250	4.61	16.95	0.23	69.55	1.96	3.88	1.30	0.05	0.17	0.03	98.73
LP16_32	125-250	4.69	14.78	0.07	73.28	2.49	2.61	0.95	0.05	0.21	0.03	99.18
LP16_32	125-250	4.03	13.72	0.11	74.13	3.05	2.03	1.03	0.07	0.28	0.03	98.48
LP16_32	125-250	3.57	10.30	0.09	76.04	2.50	1.17	1.37	0.07	0.29	0.05	95.46
LP16_32	125-250	5.29	14.09	0.06	74.51	2.01	2.22	1.04	0.07	0.27	0.04	99.58
LP16_32	125-250	3.68	11.74	0.10	64.65	1.84	1.67	1.16	0.06	0.19	0.03	85.13
LP16_32	125-250	4.09	14.31	0.17	72.31	2.05	2.34	1.15	0.05	0.17	0.05	96.68
LP16_32	125-250	5.38	15.97	0.08	69.90	1.62	2.86	1.11	0.05	0.20	0.02	97.19
LP16_32	125-250	4.01	12.84	0.24	74.70	2.64	1.66	2.21	0.08	0.39	0.07	98.83
LP16_32	125-250	5.27	15.27	0.09	70.58	1.67	3.31	0.97	0.06	0.18	0.03	97.43
LP16_32	125-250	5.02	15.23	0.26	71.60	2.60	2.50	1.29	0.06	0.22	0.06	98.83
LP16_32	125-250	5.25	15.72	0.07	69.89	1.58	3.40	0.75	0.05	0.14	0.02	96.86
LP16_32	125-250	4.94	15.25	0.05	65.87	1.38	3.19	1.04	0.08	0.17	0.02	91.99
LP16_57	63-250	4.46	13.32	0.12	77.69	2.72	1.43	0.92	0.08	0.22	0.03	100.99
LP16_57	63-250	4.35	13.50	0.13	76.98	2.57	1.58	0.77	0.09	0.22	0.03	100.21
LP16_57	63-250	3.78	11.48	0.31	78.70	2.77	1.09	1.56	0.09	0.25	0.06	100.10
LP16_57	63-250	4.35	11.94	0.03	81.03	2.29	1.44	0.72	0.07	0.10	0.02	101.99
LP16_57	63-250	4.43	12.69	0.02	83.04	0.80	2.24	0.13	0.01	0.07	0.00	103.42
LP16_57	63-250	4.21	15.66	0.02	75.96	6.50	0.45	0.18	0.02	0.08	0.00	103.04
LP16_57	63-250	4.37	13.49	0.05	76.55	0.90	2.94	0.23	0.07	0.07	0.01	98.67
LP16_57	63-250	5.73	17.91	0.02	69.02	1.26	4.43	0.63	0.04	0.08	0.02	99.14
LP16_57	63-250	5.93	19.56	0.05	66.39	2.61	4.07	0.52	0.06	0.13	0.01	99.33
LP16_57	63-250	4.38	15.93	0.43	70.13	2.77	2.62	1.59	0.06	0.15	0.08	98.14
LP16_57	63-250	6.29	17.87	0.16	69.28	1.54	3.70	1.06	0.05	0.11	0.07	100.14
LP16_57	63-250	4.82	14.94	0.05	66.35	3.42	2.88	0.65	0.08	0.14	0.02	93.37

5. Supplementary References

- Bennion, H., Sayer, C.D., Tibby, J., Carrick, H.J., Smol, J.P., and Stoermer, E.F. (2010). "Diatoms as indicators of environmental change in shallow lakes," in *The Diatoms*, eds. E.F. Stoermer & J.P. Smol. 2 ed (Cambridge: Cambridge University Press), 152-173.
- Bertrand, S., Araneda, A., Vargas, P., Jana, P., Fagel, N., and Urrutia, R. (2012). Using the N/C ratio to correct bulk radiocarbon ages from lake sediments: Insights from Chilean Patagonia. *Quaternary Geochronology* 12, 23-29.
- Bishop, T. (2021). itraxR: Itrax Data Analysis Tools. <https://CRAN.R-project.org/package=itraqR>.
- Blaauw, M., and Christen, J.A. (2011). Flexible paleoclimate age-depth models using an autoregressive gamma process. *Bayesian Analysis* 6, 457-474.
- Blaikie, J. (2020). *Palaeoenvironmental reconstruction of Late Glacial-Holocene environmental change for Patagonia, southern South America*. Unpublished PhD thesis. PhD.
- Brown, E.T. (2011). Lake Malawi's response to "megadrought" terminations: Sedimentary records of flooding, weathering and erosion. *Palaeogeography, Palaeoclimatology, Palaeoecology* 303, 120-125.
- Campos, H., Soto, D., Parra, O., Steffen, W., and Aguero, G. (1995). Limnological studies of Amarga Lagoon, Chile: A saline lake in Patagonian South America. *International Journal of Salt Lake Research* 4, 301-314.
- Croudace, I.W., Rindby, A., and Rothwell, R.G. (2006). "ITRAX:descriptions and evaluation of new mulitfunction X-ray scanner," in *New Techniques in Sediment Core Analysis*, ed. R.G. Rothwell. G), 51-63.
- Davies, B.J., Darvill, C.M., Lovell, H., Bendle, J.M., Dowdeswell, J.A., Fabel, D., García, J.-L., Geiger, A., Glasser, N.F., Gheorghiu, D.M., Harrison, S., Hein, A.S., Kaplan, M.R., Martin, J.R.V., Mendelova, M., Palmer, A., Pelto, M., Rodés, Á., Sagredo, E.A., Smedley, R.K., Smellie, J.L., and Thorndycraft, V.R. (2020). The evolution of the Patagonian Ice Sheet from 35 ka to the present day (PATICE). *Earth-Science Reviews* 204, 103152.
- Davies, S.J., Lamb, H.F., and Roberts, S.J. (2015). "Micro-XRF Core Scanning in Palaeolimnology: Recent Developments," in *Micro-XRF Studies of Sediment Cores*, eds. I.W. Croudace & R.G. Rothwell. (Dordrecht: Springer Netherlands), 189-226.
- Einarsson, Á., Stefánsdóttir, G., Jóhannesson, H., Ólafsson, J.S., Már Gíslason, G., Wakana, I., Gudbergsson, G., and Gardarsson, A. (2004). The ecology of Lake Myvatn and the River Laxá: Variation in space and time. *Aquatic Ecology* 38, 317-348.
- Farias, M.E., Contreras, M., Rasuk, M.C., Kurth, D., Flores, M.R., Poire, D.G., Novoa, F., and Visscher, P.T. (2014). Characterization of bacterial diversity associated with microbial mats, gypsum evaporites and carbonate microbialites in thalassic wetlands: Tebenquiche and La Brava, Salar de Atacama, Chile. *Extremophiles* 18, 311-329.
- Finkelstein, S.A., and Gajewski, K. (2008). Responses of Fragilaroid-dominated diatom assemblages in a small Arctic lake to Holocene climatic changes, Russell Island, Nunavut, Canada. *Journal of Paleolimnology* 40, 1079-1095.
- Fontijn, K., Lachowycz, S.M., Rawson, H., Pyle, D.M., Mather, T.A., Naranjo, J.A., and Moreno-Roa, H. (2014). Late Quaternary tephrostratigraphy of southern Chile and Argentina. *Quaternary Science Reviews* 89, 70-84.
- García, J.-L., Hall, B.L., Kaplan, M.R., Vega, R.M., and Strelin, J.A. (2014). Glacial geomorphology of the Torres del Paine region (southern Patagonia): Implications for glaciation, deglaciation and paleolake history. *Geomorphology* 204, 599-616.

- Grimm, E.C. (1987). CONISS: a FORTRAN 77 program for stratigraphically constrained cluster analysis by the method of incremental sum of squares. *Computers & Geosciences* 13, 13-35.
- Grimm, E.C., Maher Jr, L.J., and Nelson, D.M. (2009). The magnitude of error in conventional bulk-sediment radiocarbon dates from central North America. *Quaternary Research* 72, 301-308.
- Grinsted, A., Moore, J.C., and Jevrejeva, S. (2004). Application of the cross wavelet transform and wavelet coherence to geophysical time series. *Nonlinear Processes in Geophysics* 11, 561-566.
- Guerrero, J.M., and Echenique, R.O. (2002). Cyclostephanos Patagonicus sp. Nov., a New Freshwater Diatom from Western Patagonia (Argentina). *Diatom Research* 17, 141-151.
- Gunn, D.E., and Best, A.I. (1998). A new automated nondestructive system for high resolution multi-sensor core logging of open sediment cores. *Geo-Marine Letters* 18, 70-77.
- Hodell, D.A., Turchyn, A.V., Wiseman, C.J., Escobar, J., Curtis, J.H., Brenner, M., Gilli, A., Mueller, A.D., Anselmetti, F., Ariztegui, D., and Brown, E.T. (2012). Late Glacial temperature and precipitation changes in the lowland Neotropics by tandem measurement of $\delta^{18}\text{O}$ in biogenic carbonate and gypsum hydration water. *Geochimica et Cosmochimica Acta* 77, 352-368.
- Hodgson, D.A., Roberts, S.J., Bentley, M.J., Carmichael, E.L., Smith, J.A., Verleyen, E., Vyverman, W., Geissler, P., Leng, M.J., and Sanderson, D.C.W. (2009). Exploring former subglacial Hodgson Lake, Antarctica. Paper II: palaeolimnology. *Quaternary Science Reviews* 28, 2310-2325.
- Hogg, A.G., Heaton, T.J., Hua, Q., Palmer, J.G., Turney, C.S.M., Southon, J., Bayliss, A., Blackwell, P.G., Boswijk, G., Bronk Ramsey, C., Pearson, C., Petchey, F., Reimer, P., Reimer, R., and Wacker, L. (2020). SHCal20 Southern Hemisphere Calibration, 0–55,000 Years cal BP. *Radiocarbon* 62, 759-778.
- Hua, Q., Barbetti, M., and Rakowski, A.Z. (2013). Atmospheric radiocarbon for the period 1950-2010. *Radiocarbon* 55, 1–14.
- Jouve, G., Francus, P., Lamoureux, S., Provencher-Nolet, L., Hahn, A., Haberzettl, T., Fortin, D., and Nuttin, L. (2013). Microsedimentological characterization using image analysis and μ -XRF as indicators of sedimentary processes and climate changes during Lateglacial at Laguna Potrok Aike, Santa Cruz, Argentina. *Quaternary Science Reviews* 71, 191-204.
- Juggins, S. (2007). "C2 Version 1.5 User Guide. Software for ecological and palaeoecological data analysis and visualisation". (Newcastle University).
- Juggins, S. (2012). Rioja: Analysis of Quaternary Science Data, R package version (0.8-5).
- Kylander, M.E., Ampel, L., Wohlfarth, B., and Veres, D. (2011). High-resolution X-ray fluorescence core scanning analysis of Les Echets (France) sedimentary sequence: new insights from chemical proxies. *Journal of Quaternary Science* 26, 109-117.
- Lauterbach, S., Brauer, A., Andersen, N., Danielopol, D.L., Dulski, P., Hüls, M., Milecka, K., Namiotko, T., Obremska, M., and Von Grafenstein, U. (2011). Environmental responses to Lateglacial climatic fluctuations recorded in the sediments of pre-Alpine Lake Mondsee (northeastern Alps). *Journal of Quaternary Science* 26, 253-267.
- Löwemark, L., Chen, H.F., Yang, T.N., Kylander, M., Yu, E.F., Hsu, Y.W., Lee, T.Q., Song, S.R., and Jarvis, S. (2011). Normalizing XRF-scanner data: A cautionary note on the interpretation of high-resolution records from organic-rich lakes. *Journal of Asian Earth Sciences* 40, 1250-1256.
- Mansilla, C.A., McCulloch, R.D., and Morello, F. (2016). Palaeoenvironmental change in Southern Patagonia during the Lateglacial and Holocene: Implications for forest refugia

- and climate reconstructions. *Palaeogeography, Palaeoclimatology, Palaeoecology* 447, 1-11.
- Mansilla, C.A., Mcculloch, R.D., and Morello, F. (2018). The vulnerability of the Nothofagus forest-steppe ecotone to climate change: Palaeoecological evidence from Tierra del Fuego (~53°S). *Palaeogeography, Palaeoclimatology, Palaeoecology* 508, 59-70.
- Mcculloch, R.D., Bentley, M.J., Tipping, R.M., and Clapperton, C.M. (2005). Evidence for late-glacial ice dammed lakes in the central Strait of Magellan and Bahia Inutil, southernmost South America. *Geografiska Annaler Series a-Physical Geography* 87A, 335-362.
- Mcculloch, R.D., Blaikie, J., Jacob, B., Mansilla, C.A., Morello, F., De Pol-Holz, R., San Román, M., Tisdall, E., and Torres, J. (2020). Late glacial and Holocene climate variability, southernmost Patagonia. *Quaternary Science Reviews* 229, 106131.
- Mcculloch, R.D., and Davies, S.J. (2001). Late-glacial and Holocene palaeoenvironmental change in the central Strait of Magellan, southern Patagonia. *Palaeogeography Palaeoclimatology Palaeoecology* 173, 143-173.
- Mcculloch, R.D., Figuerero Torres, M.J., Mengoni Goñalons, G.L., Barclay, R., and Mansilla, C. (2017). A Holocene record of environmental change from Río Zeballos, central Patagonia. *The Holocene* 27, 941-950.
- Mcculloch, R.D., Mansilla, C.A., Martin, F., Borrero, L., Staff, R.A., and Tisdall, E.W. (2021). The nature and timing of landscape change at Cerro Benítez, Última Esperanza, southern Patagonia (52°S): New insights into the history of megafaunal extinctions and human occupation. *Quaternary International* 601, 116-129.
- Mcculloch, R.D., Mansilla, C.A., Morello, F., De Pol-Holz, R., San Román, M., Tisdall, E., and Torres, J. (2019). Late glacial and Holocene landscape change and rapid climate and coastal impacts in the Canal Beagle, southernmost Patagonia. *Journal of Quaternary Science* 34, 674-684.
- Melles, M., Brigham-Grette, J., Minyuk, P.S., Nowaczyk, N.R., Wennrich, V., Deconto, R.M., Anderson, P.M., Andreev, A.A., Coletti, A., Cook, T.L., Haltia-Hovi, E., Kukkonen, M., Lozhkin, A.V., Rosen, P., Tarasov, P., Vogel, H., and Wagner, B. (2012). 2.8 million years of Arctic climate change from Lake El'gygytgyn, NE Russia. *Science* 337, 315-320.
- Mueller, A.D., Islebe, G.A., Hillesheim, M.B., Grzesik, D.A., Anselmetti, F.S., Ariztegui, D., Brenner, M., Curtis, J.H., Hodell, D.A., and Venz, K.A. (2017). Climate drying and associated forest decline in the lowlands of northern Guatemala during the late Holocene. *Quaternary Research* 71, 133-141.
- Oksanen, J. (2014). "Vegan: Community Ecology Package. R package version 2.3-0.". (<http://cran.r-project.org/web/packages/vegan/index.html>).
- Olsen, J., Anderson, N.J., and Leng, M.J. (2013). Limnological controls on stable isotope records of late-Holocene palaeoenvironment change in SW Greenland: a paired lake study. *Quaternary Science Reviews* 66, 85-95.
- Ramsey, C.B. (2009). Bayesian Analysis of Radiocarbon Dates. *2009*, 24.
- Roberts, S.J., Monien, P., Foster, L.C., Loftfield, J., Hocking, E.P., Schnetger, B., Pearson, E.J., Juggins, S., Fretwell, P., Ireland, L., Ochyra, R., Haworth, A.R., Allen, C.S., Moreton, S.G., Davies, S.J., Brumsack, H.J., Bentley, M.J., and Hodgson, D.A. (2017). Past penguin colony responses to explosive volcanism on the Antarctic Peninsula. *Nat Commun* 8, 14914.
- Rothwell, R.G., and Croudace, I.W. (2015). "Micro-XRF Studies of Sediment Cores: A Perspective on Capability and Application in the Environmental Sciences," in *Micro-XRF Studies of Sediment Cores*, eds. I.W. Croudace & R.G. Rothwell. (Dordrecht: Springer Netherlands), 1-21.

- Rumrich, U., Lange-Bertalot, H., and Rumrich, M. (2000). Diatoms of the Andes: from Venezuela to Patagonia/Tierra del Fuego. *Iconographia Diatomologica* 9.
- Sagredo, E.A., Moreno, P.I., Villa-Martínez, R., Kaplan, M.R., Kubik, P.W., and Stern, C.R. (2011). Fluctuations of the Última Esperanza ice lobe (52° S), Chilean Patagonia, during the last glacial maximum and termination 1. *Geomorphology* 125, 92-108.
- Saunders, K.M., Roberts, S.J., Perren, B., Butz, C., Sime, L., Davies, S., Van Nieuwenhuyze, W., Grosjean, M., and Hodgson, D.A. (2018). Holocene dynamics of the Southern Hemisphere westerly winds and possible links to CO₂ outgassing. *Nature Geoscience* 11, 650-655.
- Smith, R.E., Smith, V.C., Fontijn, K., Gebhardt, A.C., Wastegård, S., Zolitschka, B., Ohlendorf, C., Stern, C., and Mayr, C. (2019). Refining the Late Quaternary tephrochronology for southern South America using the Laguna Potrok Aike sedimentary record. *Quaternary Science Reviews* 218, 137-156.
- Solari, M.A., Le Roux, J.P., Herve, F., Airo, A., and Calderon, M. (2012). Evolution of the Great Tehuelche Paleolake in the Torres del Paine National Park of Chilean Patagonia during the Last Glacial Maximum and Holocene. *Andean Geology* 39, 1-21.
- Stern, C., Moreno, P., Henríquez, W., Villa-Martínez, R., Sagredo, E., Aravena, J., and De Pol-Holz, R. (2015). Holocene tephrochronology around Cochrane ($\sim 47^{\circ}$ S), southern Chile. *Andean Geology* 43, 1-19.
- Stevenson, R.J., Pan, Y., Stoermer, E.F., and Smol, J.P. (1999). "Assessing environmental conditions in rivers and streams with diatoms," in *The Diatoms*, eds. E.F. Stoermer & J.P. Smol. (Cambridge: Cambridge University Press), 11-40.
- Stevenson, R.J., Pan, Y., Van Dam, H., Smol, J.P., and Stoermer, E.F. (2010). "Assessing environmental conditions in rivers and streams with diatoms," in *The Diatoms*, eds. E.F. Stoermer & J.P. Smol. 2 ed (Cambridge: Cambridge University Press), 57-85.
- Wennrich, V., Minyuk, P.S., Borkhodoev, V., Francke, A., Ritter, B., Nowaczyk, N.R., Sauerbrey, M.A., Brigham-Grette, J., and Melles, M. (2014). Pliocene to Pleistocene climate and environmental history of Lake El'gygytgyn, Far East Russian Arctic, based on high-resolution inorganic geochemistry data. *Climate of the Past* 10, 1381-1399.
- Westover, K.S., Fritz, S.C., Blyakharchuk, T.A., and Wright, H.E. (2006). Diatom Paleolimnological Record of Holocene Climatic and Environmental Change in the Altai Mountains, Siberia. *Journal of Paleolimnology* 35, 519-541.
- Wilhelms-Dick, D., Westerhold, T., Röhl, U., Wilhelms, F., Vogt, C., Hanebuth, T.J.J., Römmermann, H., Kriewa, M., and Kasten, S. (2012). A comparison of mm scale resolution techniques for element analysis in sediment cores. *Journal of Analytical Atomic Spectrometry* 27, 1574-1584.